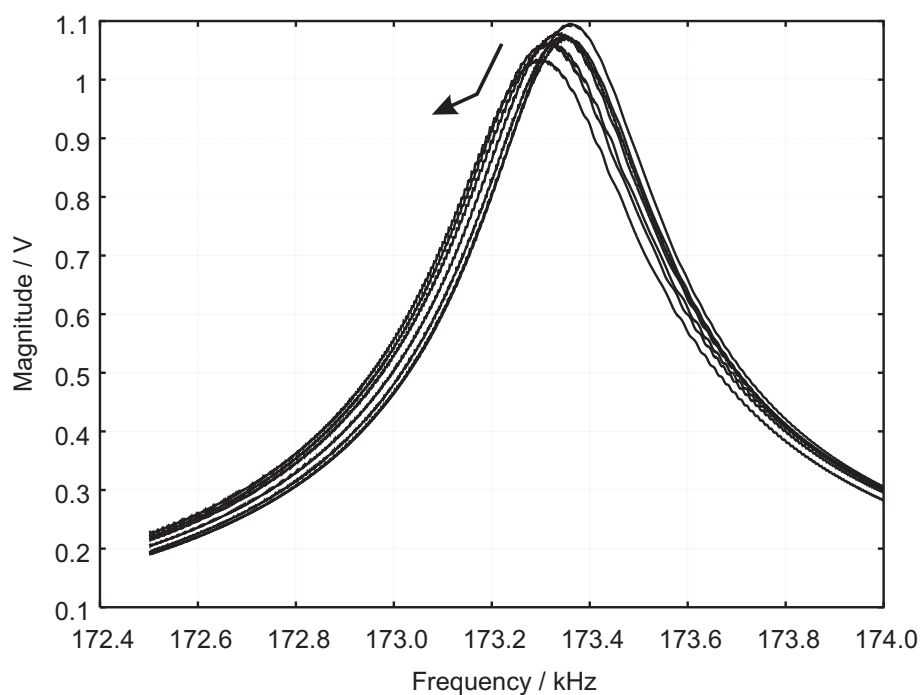


# High resolution frequency analysis in Scanning Probe Microscopy



Polichronis Lepidis



# High resolution frequency analysis in Scanning Probe Microscopy

Im Fachbereich Elektrotechnik und Informationstechnik der  
Bergischen Universität–Gesamthochschule Wuppertal

zur Erlangung des akademischen Grades eines

Doktor-Ingenieurs

genehmigte Dissertation

von

Dipl.-Ing.  
Polichronis Lepidis

aus

Schwelm

Referent: Prof. Dr. rer.nat. Ludwig Josef Balk

Korreferent: Prof. Dr. Ing. Albrecht Glasmachers

Tag der mündlichen Prüfung: 25.10.2002



*Der dritte und letzte Motivationsfaktor heißt “Unterhaltung, Vergnügen, Spaß”. Das mag banal klingen, aber Spaß ist fraglos ein außerordentlich starker Antrieb.*

*Linus Torvalds – Just for Fun*



---

## Abbreviations, variables, symbols and constants

$\alpha$	Polarizability [ $Asm^2/V$ ], Temperature coefficient [ $1/K$ ]
$\beta$	Optical amplification
$\Delta\varphi$	Phase increment
$\epsilon_0$	Electric permittivity [ $8.854 \cdot 10^{-12}C^2/Jm$ ]
$\epsilon_r$	Relative permittivity
$\gamma$	Damping coefficient
$\lambda$	Wavelength of light [ $nm$ ]
$\mu$ TMA	Micro Thermo Analysis
$\mu^i$	Self energy
$\omega$	Circular frequency [ $Hz$ ]
$\omega_0$	Resonance circular frequency [ $Hz$ ]
$\pi$	Circle constant [3.141529]
$\rho$	Specific density [ $kg/m^3$ ]
$\sigma$	Hard-sphere diameter [ $m$ ]
$\tau$	Response time [ $s$ ]
$\varphi$	Phase
$A$	Magnitude
$B$	Measurement Bandwidth [ $Hz$ ]
$C$	Capacitance [ $F$ ]
$d_{31}, d_{13}$	Piezoelectric coefficient [ $m/V$ ]
$E$	Electrical field strength [ $V/m$ ], Young's Modulus [ $98 GN/m^2$ ]
$e$	Electron's Charge [ $1.60217733 \cdot 10^{-19}As$ ]
$e_n$	Equivalent Noise Voltage Density [ $V/\sqrt{Hz}$ ]

---

$F$	Force [ $N$ ]
$f$	Frequency [ $Hz$ ]
$f_0$	Resonance Frequency [ $Hz$ ]
$f_s$	Sampling frequency [ $Hz$ ]
$G$	Temperature Gradient [ $K/s$ ]
$h$	Planck's constant [ $6.626 \cdot 10^{-34} J \cdot s$ ]
$I$	Area Moment of Inertia [ $kg \cdot m^2$ ], Electrical Current [ $A$ ], Imaginary part/output
$i_n$	Equivalent Noise Current Density [ $A/\sqrt{Hz}$ ]
$j$	Imaginary unit
$k$	Boltzman's constant [ $1.380658 \cdot 10^{-23} J/K$ ], Cantilever's spring constant [ $N/m$ ]
$L$	Inductor [ $H$ ]
$m$	Mass [ $kg$ ]
$P$	Power [ $W$ ]
$R$	Electrical Resistance [ $\Omega$ ], Photodiode Responsivity [ $A/W$ ], Real part/output
$r$	radius [ $m$ ]
$T$	Temperature [ $K$ ], Time [ $s$ ]
$T_G$	Glass Temperature/Point
$T_M$	Melting Temperature/Point
$u$	Dipole moment [ $Asm$ ]

---

$U, V$	Electrical Voltage [V]
$w$	Pair-Potential, Interaction energy [ $Nm$ ]
$X$	Real part/output
$Y$	Imaginary part/output
$x, y, z$	Spatial coordinates
AC	Alternate current
ADC	Analog to digital converter
AFM	Atomic Force Microscope/Microscopy
AGC	Automatic gain compensation
CMAC	Complex multiplier accumulator
DAC	Digital to analog converter
DC	Direct current
DDF	Digital Decimation Filter
DDS	Direct digital synthesis
DEA	Dielectric Analyzer/Analysis
DFT	Discrete Fourier Transformation
DMTA	Differential (Thermo) Mechanical Analyzer/Analysis
DSC	Differential Scanning Calorimeter/Calorimetry
DSO	Digital Sampling Oscilloscope
ECU	Electronic Control Unit
EPP	Enhanced Parallel Port
FFT	Fast Fourier Transformation
FIR	Filter with finite impulse response
FM	Frequency modulation
FSK	Frequency shift keying

---

HDF	High order decimation
HPF	High pass filter
I/V-converter	Current to Voltage Converter
IC	Integrated circuit
LIA	Lock-In Amplifier
LPF	Low pass filter
L-R	Difference signal (Left - Right)
MFM	Magnetic Force Microscope/Microscopy
NCOM	Numeric controlled oscillator / modulator
OP	Operation amplifier
PC	Personal computer
PD	Photo detector [element]
PFCS	Phase and frequency control section
PID	Proportional, Integral, Deviation [Controller]
PLL	Phase Locked Loop
PSD	Phase Sensitive Detector
PSD	Position Sensitive Detector
PWM	Pulse width modulation
PZT	Piezoelectric ceramics made of Pb, Zi, Ti
Q, q	Electric Charge [ $As$ ]
QPSK	Quad phase shift keying
SEM	Scanning Electron Microscope/Microscopy
SFFM	Scanning Friction Force Microscopy
SFM	Scanning Force Microscope/Microscopy
SNOM	Scanning Nearfield Optical Microscope

---

SNR Signal to noise ratio

SPM Scanning Probe Microscope/Microscopy

STM Scanning Tunnelling Microscope/Microscopy

T-B Difference signal (Top - Bottom)

*Multiple occurrences of certain symbols have been prevented to maintain the consistence with the conventions in different topics.*

---

# Contents

<b>1</b>	<b>Introduction</b>	<b>17</b>
<b>2</b>	<b>Fundamentals of Scanning Probe Microscopy</b>	<b>21</b>
2.1	Introduction . . . . .	21
2.2	The Pair-potential of molecules . . . . .	22
2.3	Electrostatic forces . . . . .	23
2.3.1	Charge–charge interactions . . . . .	23
2.3.2	Charge–dipole interactions . . . . .	24
2.3.3	Dipole–dipole interactions . . . . .	26
2.4	Polarization forces . . . . .	27
2.4.1	Charge–nonpolar interactions . . . . .	27
2.4.2	Dipole-induced dipole interactions . . . . .	28
2.4.3	Nonpolar-nonpolar interactions . . . . .	29
2.5	Repulsive interactions . . . . .	30
2.5.1	The hard sphere potential . . . . .	30
2.5.2	The power-law potential . . . . .	31
2.5.3	The exponential potential . . . . .	31
2.6	Generalized force theory . . . . .	31

<b>3</b>	<b>Determination of tip-sample interactions with an SPM in Dynamic Operation Mode</b>	<b>35</b>
3.1	The free vibrating cantilever . . . . .	35
3.2	Distance control in dynamic mode microscopy . . . . .	38
3.2.1	Slope detection . . . . .	38
3.2.2	Frequency modulation detection . . . . .	39
3.3	Influences of tip-sample interactions on the vibrating cantilever . . . . .	40
3.4	Determination of tip-sample interactions using a force based approach . . . . .	41
3.5	Determination of tip-sample interactions using an energy based approach . . . . .	43
3.6	Determination of polymer properties with dynamic mode SPM . . . . .	45
<b>4</b>	<b>The Scanning Probe Microscope</b>	<b>47</b>
4.1	Experimental Setup . . . . .	47
4.2	The Force Probe . . . . .	49
4.3	Detection Unit . . . . .	52
4.3.1	Optical Deflection Detection . . . . .	52
4.3.2	Photodetector and Instrumentation . . . . .	54
4.4	Modulation Unit . . . . .	62
4.4.1	Piezo-Actuator . . . . .	62
4.4.2	Signal Coupling . . . . .	65
<b>5</b>	<b>High resolution frequency analysis in Scanning Probe Microscopy</b>	<b>69</b>
5.1	Frequency analysis systems for the characterization of dynamic properties . . . . .	70
5.1.1	FFT-Spectrum-Analyzer . . . . .	70

5.1.2	Lock-In Amplifiers . . . . .	73
5.1.3	Network Analyzer . . . . .	75
5.1.4	Comparison of the different methods . . . . .	76
5.2	High resolution digital frequency analysis of dynamic properties in Scanning Probe Microscopy . . . . .	77
5.2.1	Requirements on the electronics . . . . .	78
5.2.2	Realization of the digital frequency analysis system	80
5.3	High resolution digital frequency analysis on polymers .	106
<b>6</b>	<b>Conclusion</b>	<b>113</b>

## *Contents*

---

# 1 Introduction

The invention of the Scanning Tunnelling Microscope (STM) in 1981 [1] opened the gate to a new world for the surface sciences. For the first time it was possible to visualize the surface structure of materials in the atomic scale directly. Shortly after this invention it was *"already clear that entirely new fields are opening up for the study of the structure of matter"* as the Nobel Prize Committee pointed out in their official press release, and so the inventors of the STM, Gerd Binnig and Heinrich Rohrer, were honored together with Ernst Ruska, who received the prize *"for his fundamental work in electron optics and for the design of the first electron microscope"* dating around 1930, with the Nobel Prize in Physics in 1986 [2].

Further development of the scanning probe technique overcame the major drawback of the STM, its limitation to electrical conductive samples. With the introduction of the Scanning Force Microscope (SFM), also known as Atomic Force Microscope (AFM), in 1986 the investigation range was exceeded to non conductive samples. The independence of electric conductive samples was achieved by the utilization of atomic force interactions between a needle-sharp tip, mounted

on the very end of a cantilever, and the sample as a distance dependent sensing mechanism instead of using the tunnelling current like in STM. As the spatial resolution of the SFM is in principle only limited by the sharpness of the tip, the inventors, Binnig, Quate and Gerber, predicted the achievement of atomic resolution in their first presentation of the SFM [3].

Nevertheless it took almost 10 years before an image with *true atomic resolution* of the Silicon (111)-(7x7) reconstruction was reported for the first time using an SFM [4], [5]. Instead of operating the SFM in the well established static mode<sup>1</sup> both groups chose a dynamic operation mode<sup>2</sup> [6] using a frequency modulation detection scheme [7] to perform their experiments.

Due to the nature of the atomic interaction forces, there is also a strong dependence on the chemical structure and composition of the sample. Observing the interaction forces between tip and sample, using the SFM in force spectroscopy mode [8]-[10], thus allows the detection of material specific properties. This opens up a great application field for scanning probe techniques, the characterization of materials in the nanoscale region. Particularly the detailed analysis of heterogeneous and multiphase organic materials is becoming of strong increasing interest in recent years.

The research done in this field covers the analysis of mechanical properties of polymers. Techniques like nanoindentation with the SFM

---

<sup>1</sup>Also often referred as contact mode.

<sup>2</sup>A lot of different terms are used synonymical for similar experimental setups.

In this work dynamic mode will be used as generic term for noncontact mode, tapping mode and similar dynamic operation modes.

---

[11] as well as the Pulsed Force Operation Mode [12] were successfully used for the determination of elastic and viscoelastic properties of polymers [13]. The micro mechanics of single molecules were also analyzed with SPM techniques, e.g. trying to observe the unfolding forces of protein chains [14]-[15]. Separation of different polymer phases of composites could be obtained by the use of nanomapping techniques [16]. Further attempts were made to develop techniques for the characterization of thermal and thermomechanical properties [17], gaining special focus on the determination of the glass transition point of polymers using scanning probe techniques [18]-[22].

Most of these works were carried out by extending a commercial SFM system with additional hardware or even by using self-constructed scanning probe instruments, as the commercial available instruments can not cover every experimental purpose.

The resulting solutions can be classified either as low-cost solutions, which lack often in terms of accuracy, resolution and comfort, or as high-end solutions, which are often very expensive and such powerful, that skilled operators are demanded for routinely operation. Both approaches are not wholeheartedly qualified to spread the use of SPM based methods in classical environments of polymer investigation. An instrument with simplicity of operation but despite the ability of accurate and reliant data acquisition is thus still desired to make SPM based techniques accessible as a standard tool in polymer characterization.

In this work, a new developed system for performing force spectroscopy analysis using the dynamic mode of an SFM is presented.

The motivation for this frequency analysis system is the reliable acquisition of the dynamic behavior of the tip-sample system with high resolution as a function of parameters like temperature or pressure. The observation of the dynamic properties of the tip-sample systems enables the investigation of mechanical and thermomechanical properties for a great variety of material compositions. Compared to others existing frequency analysis systems, a major design aim of the system is the development of an affordable, ease-of-use add-on which can be attached to any existing scanning probe microscope working on a high level of automation.

The present work is structured into the following sections:

A brief introduction in the fundamental interactions in Scanning Probe Microscopy is presented in chapter 2, followed by a special focus on the dynamic mode and the determination of tip-sample interactions in dynamic mode in chapter 3. The realization and setup of a Scanning Probe Microscope is presented in chapter 4, to form a background for the understanding of SPM-related issues which may appear into the scope of this work. Chapter 5 gives an overview over possible implementation schemes of frequency analysis systems, emphasizing in short terms advantages and withdraws of the different techniques, and presents in the following the realization of the chosen concept under consideration of SPM-related issues in detail, demonstrating the performance of the system in respect to different applications, like the investigation of microscopic polymer properties. With a brief summary in Chapter 6 this work will be closed.

# 2 Fundamentals of Scanning Probe Microscopy

## 2.1 Introduction

Every member of the Scanning Probe Microscope family operates according to the same principle. A probe is scanned over the surface of the sample to be investigated. The image is formed by assigning the interaction between the probe and the sample to a given location of the sample surface. Generally speaking, this means that every picture element  $p$  is given by the function

$$p = f(x, y, i) \tag{2.1}$$

where  $x, y$  determine the location and  $i$  the interaction at this point.

The classification of the different types of Scanning Probe Microscopes is done in dependence on the interaction mechanism. Using this definition, the Scanning Electron Microscope (SEM) can be considered as one of the first members of the SPM family, followed by the Scanning Tunnelling Microscope around 30 years later [2]. The interaction

mechanism in Scanning Tunnelling Microscopy is a tunnelling current, which flows when an electrically conductive tip is positioned close to an electrically conductive sample and a voltage is applied between both. For the Scanning Force Microscope the interaction mechanism is the occurrence of intermolecular forces between two bodies in near proximity to each other. A brief overview of the theory of intermolecular and surface forces is presented in the following sections, while a detailed description is provided in [46].

## 2.2 The Pair-potential of molecules

Every individual molecule brought inside a medium has a so-called *cohesive* or *self-energy*  $\mu^i$  which can be described by the sum of all interactions of this molecule with the molecules of the surrounding medium. Assuming a spherical medium with radius  $r$  and a number density of the molecule of this medium of  $\rho$ , the self-energy can be given as

$$\mu^i = \int_{\sigma}^{\infty} w(r) \rho 4\pi r^2 dr , \quad (2.2)$$

where  $\sigma$  is the so-called *hard-sphere* diameter of the molecules and  $w(r)$  defines the interaction energy or *pair-potential* between an individual molecule and one molecule of the medium. This interaction potential forms the basis for the treatment of intermolecular forces and is related to the force between these two molecules as

$$F = -\frac{\partial w(r)}{\partial r} . \quad (2.3)$$

Intermolecular forces can be loosely classified into three categories. Purely electrostatic forces, arising from the interaction between

charges, polarization forces arising from induced dipole moments by electric fields of nearby charges and forces arising due to quantum mechanical interactions. This classification should not be considered as the solely possible one, as some types of forces are not included in this classes and other types, like van der Waals forces, do not fit easily in this classification.

## 2.3 Electrostatic forces

### 2.3.1 Charge–charge interactions

The interaction energy between two charges  $Q_1, Q_2$  is given by

$$w(r) = \frac{Q_1 Q_2}{4\pi\epsilon_0\epsilon_r r} , \quad (2.4)$$

the well-known Coulomb's law, with  $\epsilon_0$ <sup>1</sup> as the permittivity of free space,  $\epsilon_r$  the relative permittivity of the medium and  $r$  the distance between the two charges.

The calculation of the force is in this case very easy and given by

$$F(r) = -\frac{dw(r)}{dr} = \frac{Q_1 Q_2}{4\pi\epsilon_0\epsilon_r r^2} . \quad (2.5)$$

For repulsive forces the charges have the same sign and  $w(r)$  and  $F(r)$  are positive, while for attractive forces, i.e. for unlike charges, the pair-potential and the interaction force are both negative. As this interaction mechanism is very strong, about 200 times greater than the thermal energy  $kT$  at 300K [46]<sup>2</sup>, and the distance dependency is with

---

<sup>1</sup> $\epsilon_0 = 8.854 \cdot 10^{-12} C^2 / (Jm)$

<sup>2</sup> $k = 1.380658 \cdot 10^{-23} J/K$

a power of 2 comparably small<sup>3</sup> (see following sections), Coulomb's forces can play an important role in Scanning Force Microscopy.

### 2.3.2 Charge–dipole interactions

Charge–charge interaction as described in section 2.3.1 are typical interactions between ions. Most molecules however do not carry a *net charge*, rather they are forming a permanent electric dipole by drawing single electrons, e.g. from a hydrogen atom, to the atom bonded to the hydrogen. The dipole moment  $u$  of such *polar molecules* is defined as

$$u = q \cdot l, \quad (2.6)$$

where  $l$  is the distance between the two charges  $+q$  and  $-q$ , as shown in Fig. 2.1. The interaction of a fixed dipole with a single charge can be described as the superposition of the interaction of the charge with every single charge of the dipole.

$$w(r) = w(r, \vartheta) = -\frac{Qq}{4\pi\epsilon_0\epsilon_r} \left( \frac{1}{AB} - \frac{1}{AC} \right) \quad (2.7)$$

---

<sup>3</sup>It should be mentioned at this point, that this is actually only true for two isolated ions. Ions built in a lattice or inside a solution will always have other ions of opposite charge nearby them screening the electric field and making the decay more rapid.

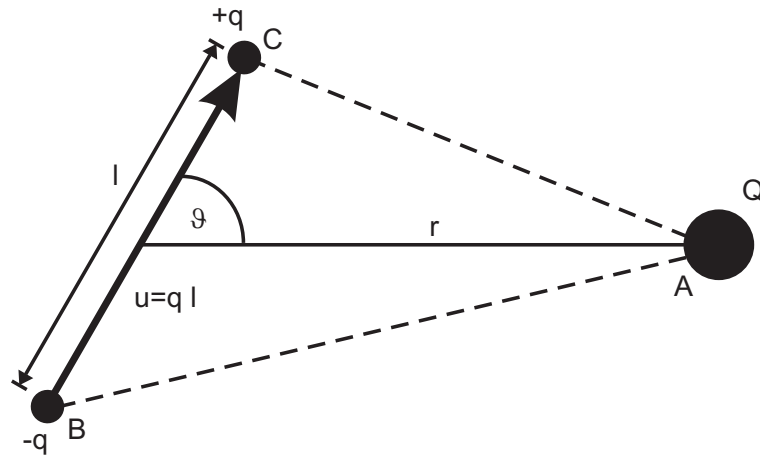


Figure 2.1: Charge–Dipole Interaction

Evaluating Eq. 2.7 using fundamental geometrical considerations, the charge–dipole interaction energy can be written, for  $r \gg l$ , approximately as

$$w(r) = w(r, \vartheta) = -\frac{Qu \cos(\vartheta)}{4\pi\epsilon_0\epsilon_r r^2}. \quad (2.8)$$

If the angular dependence of the interaction energy becomes smaller than the thermal energy  $kT$ , dipoles can rotate more or less freely. The angle-averaged interaction energy for the charge–dipole interaction is given in this case, i.e. for

$$kT > \frac{Qu}{4\pi\epsilon_0\epsilon_r r^2}, \quad (2.9)$$

approximately by

$$w(r) = w(r, T) = -\frac{Q^2 u^2}{6(4\pi\epsilon_0\epsilon_r)^2 kT r^4}, \quad (2.10)$$

which is highly temperature dependent.

### 2.3.3 Dipole–dipole interactions

The interaction energy between two dipoles at a distance  $r$  apart from each other with dipole moments  $u_1$  and  $u_2$ , as given by Fig. 2.2,

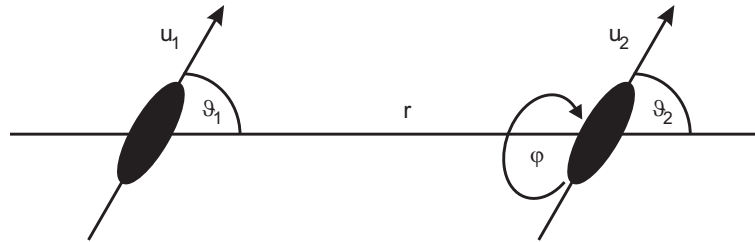


Figure 2.2: Dipole–Dipole Interaction

can be calculated in a manner analogous to the previous section, leading to an interaction energy of

$$w(r) = w(r, \vartheta_1, \vartheta_2, \varphi) \quad (2.11)$$

$$= -\frac{u_1 u_2}{4\pi\epsilon_0\epsilon_r r^3} (2 \cos(\vartheta_1) \cos(\vartheta_2) - \sin(\vartheta_1) \sin(\vartheta_2) \cos(\varphi)) \quad (2.12)$$

In further analogy to charge-dipole interactions, the dipoles are free to rotate for an interaction energy smaller than the thermal energy  $kT$ , resulting in an angle-averaged interaction energy of

$$w(r) = w(r, T) = -\frac{u_1^2 u_2^2}{3(4\pi\epsilon_0\epsilon_r)^2 kT r^6} . \quad (2.13)$$

This, also strong temperature dependent, term is known as the *Keesom interaction* and contributes as one of three important components to the total van der Waals interaction.

## 2.4 Polarization forces

### 2.4.1 Charge–nonpolar interactions

Beside molecules with permanent dipoles, molecules can possess dipoles, which are induced by the electrical field of nearby charges. Molecules with induced dipoles can be characterized by their induced dipole moment  $u_{ind}$ , which is given as

$$u_{ind} = \alpha E . \quad (2.14)$$

$E$  is defining here the local electrical field-strength,  $\alpha$  the *polarizability*. Different mechanisms can cause the arising of polarizability. Electron polarizability e.g. is arising from the displacement of the electron cloud, with charge  $-q$ , relative to the nucleus by a distance  $l$ , due to the influence of the electric field of a nearby charge. The induced dipole moment can be written in this case as

$$u_{ind} = \alpha_0 E = ql , \quad (2.15)$$

where  $\alpha_0$  defines the electron polarizability, which is proportional to the effective volume of the atom or molecule. The interaction of such an nonpolar molecule with a charge, e.g. an ion, will lead to an energy given by

$$w(r) = -\frac{1}{2}\alpha E^2 = -\frac{\alpha Q^2}{2(4\pi\epsilon_0\epsilon_r)^2 r^4} . \quad (2.16)$$

### Polarizability of polar molecules

Considering a freely rotating dipolar molecule, with a time-averaged dipole moment of zero, a nearby charge will perturb this polar molecule,

giving rise to an *orientational polarizability* which is given by

$$\alpha_{orient} = \frac{u^2}{3kT} \quad (2.17)$$

leading to a total polarizability of a polar molecule of

$$\alpha = \alpha_0 + \alpha_{orient} . \quad (2.18)$$

The pair potential for these molecules is given therefore as

$$w(r) = -\frac{1}{2}\alpha E^2 = -\frac{Q^2}{2(4\pi\epsilon_0\epsilon_r)^2 r^4} \left( \alpha_0 + \frac{u^2}{3kT} \right) . \quad (2.19)$$

### 2.4.2 Dipole-induced dipole interactions

The interaction between polar and nonpolar molecules is in analogy to the previously described interactions. The electric field of a fixed permanent dipole, as described in Fig. 2.2, is given by

$$E = \frac{u\sqrt{1+3\cos^2(\vartheta)}}{4\pi\epsilon_0\epsilon_r r^3} . \quad (2.20)$$

The interaction energy is thus

$$w(r) = -\frac{1}{2}\alpha E^2 = -\frac{\alpha u^2(1+3\cos^2(\vartheta))}{2(4\pi\epsilon_0\epsilon_r)^2 r^6} . \quad (2.21)$$

With an average angle of  $\cos^2(\vartheta) = 1/3$  this leads to

$$w(r) = -\frac{\alpha u^2}{(4\pi\epsilon_0\epsilon_r)^2 r^6} . \quad (2.22)$$

The more general case, the interaction of two dipoles, where both possess a permanent dipole and polarize themselves each other, is given by

$$w(r) = -\frac{(\alpha_2 u_1^2) + (\alpha_1 u_2^2)}{(4\pi\epsilon_0\epsilon_r)^2 r^6} . \quad (2.23)$$

This is known as the *Debye interaction energy* which has, as the Keesom energy referred in Eq. 2.13, a dependence with a power of six to the distance and gives the second important contribution to the van der Waals forces.

### 2.4.3 Nonpolar-nonpolar interactions

The third important contribution to the van der Waals forces is caused by nonpolar-nonpolar interactions. Though difficult to describe, due to their quantum mechanical origin, these so-called *dispersion forces* play an important role, as they are always present and responsible for a lot of phenomena like adhesion, surface tension and others. A rather simple model for explaining this type of interaction is based on the interaction of fluctuating dipoles. In this model, every atom is representing an instantaneous dipole with a dipole moment given by

$$u = a_0 e \quad (2.24)$$

where  $e$  is the electron's charge and  $a_0$  as the so-called first Bohr radius given by

$$a_0 = \frac{e^2}{2(4\pi\epsilon_0 h f)}, \quad (2.25)$$

where  $h$  is the Planck constant and  $f$  the orbiting frequency of the electron. The interaction energy of two of these atomic dipoles can therefore be calculated as presented in Sec. 2.4.2 and is given approximately as

$$w(r) \approx -\frac{\alpha^2 h f}{(4\pi\epsilon_0)^2 r^6}, \quad (2.26)$$

The *London equation*, derived around 1930 using quantum mechanical perturbation theory for the determination of the dispersion forces, gives for the dispersion energy between two identical atoms

$$w(r) = -\frac{3}{4} \frac{\alpha^2 h f}{(4\pi\epsilon_0)^2 r^6} \quad (2.27)$$

and for two dissimilar atoms

$$w(r) = -\frac{3}{2} \frac{\alpha_1^2 \alpha_2^2}{(4\pi\epsilon_0)^2 r^6} \frac{h f_1 f_2}{f_1 + f_2}, \quad (2.28)$$

which is in good agreement with the simple Bohr atom model.

## 2.5 Repulsive interactions

For very small interatomic distances, when the electron clouds of atoms overlap, a strong repulsive force is arising limiting the minimum possible interatomic distance. Repulsive forces belong to the class of quantum mechanical forces, caused e.g. by Pauli's exclusion principle. As there is no general equation for the description of their interaction energy, different empirical potential functions have been introduced to allow mathematical treatment of this interaction type. The most common of these potentials are the *hard sphere potential*, the *inverse power-law potential* and the *exponential potential* [46].

### 2.5.1 The hard sphere potential

Using the hard sphere potential the atoms are considered as hard, incompressible spheres. The potentials therefore becomes infinite at a certain interatomic distance, the hard sphere diameter  $\sigma$ .<sup>4</sup> The interaction energy describing this behavior is given by

$$w(r) = + \left( \frac{\sigma}{r} \right)^n \quad (2.29)$$

with  $n \rightarrow \infty$  for  $r \rightarrow \sigma$ . For distances  $r > \sigma$  the pair-potential is effectively zero, while for  $r < \sigma$  it goes to infinity.

---

<sup>4</sup>Usually twice the van der Waals radius.

### 2.5.2 The power-law potential

The power-law potential is similar to the hard sphere potential and also given as

$$w(r) = + \left( \frac{\sigma}{r} \right)^n, \quad (2.30)$$

with the difference of  $n < \infty$ , typically between 9 and 16. This makes the increase of the repulsive potential more softly, allowing the modelling of a finite compressibility of atoms.

### 2.5.3 The exponential potential

A different approach is taken by the exponential potential defining the interaction energy as

$$w(r) = +ce^{-r/\sigma_0}, \quad (2.31)$$

where  $c$  and  $\sigma_0$  are adjustable constants.

## 2.6 Generalized force theory

Concluding the so far presented cases from the electrical engineers point-of-view, the fundamental intermolecular interactions can be described using electrostatic theory under consideration of polarization effects. For great distances between two interacting molecular objects, if no voltage is applied, the effective force is attractive and dominated by the van der Waals forces.

Van der Waals forces can be described using the Keesom, Debye and

London dispersion potential functions by

$$w_{vdW}(r, T) = - \frac{\frac{u_1^2 u_2^2}{3kT} + (\alpha_2 u_1^2) + (\alpha_1 u_2^2) + \frac{3\alpha_1^2 \alpha_2^2 h f_1 f_2}{2(f_1 + f_2)}}{(4\pi\epsilon_0\epsilon_r)^2 r^6}, \quad (2.32)$$

with the characteristic distance dependency with a power of six but also a dependency on temperature. For small distances between two objects, repulsive force components have to be considered as well. The potential functions causing these forces are not easy to describe using simple macroscopic models. Empirical functions have been introduced therefore for description.

The *total intermolecular pair-potential* is obtained by summing all involved attractive and repulsive potentials. As usually more than two molecular objects are involved in a typical tip-sample interaction, the amount of interactions become easily too complicated to treat them individually, and generalized potential functions for the total intermolecular pair-potential have been introduced to describe the general behavior. One well accepted and widely used is the so-called *Lennard-Jones* or "6-12"<sup>5</sup> potential, which is given by

$$w(r) = \frac{C_{rep}}{r^{12}} - \frac{C_{attr}}{r^6}. \quad (2.33)$$

$C_{attr}$  and  $C_{rep}$  are constants describing the attractive and repulsive force components. According to Eq. 2.3, the force function for this potential is given by

$$F(r) = - \frac{\partial w}{\partial r} = \frac{C'_{attr}}{r^7} - \frac{C'_{rep}}{r^{13}}, \quad (2.34)$$

which is plotted in Fig. 2.3 and describes the characteristic behavior.

---

<sup>5</sup>According to the involved power factors

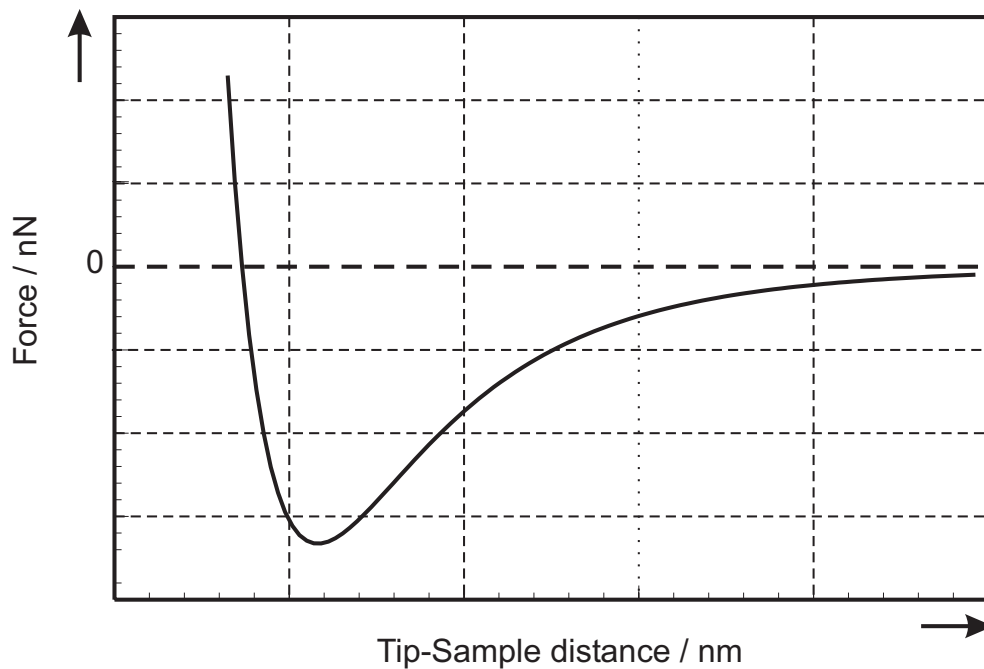


Figure 2.3: Force distance dependence as given by the Lennard-Jones potential

For great distances, i.e. a tip position *far away* from the sample, where the long-range forces are acting, the effective force between tip and sample is attractive. If the tip moves closer to the sample the influence of the attractive forces is increasing. At the point of inflection the influence of repulsive forces becomes stronger and the curve changes its direction. Shortly after this point, the force-distance curve loses its monotonic properties. Moving the tip closer to the sample leads to a further increasing influence of the repulsive forces and the effective force becomes repulsive.

## *2 Fundamentals of Scanning Probe Microscopy*

---

# 3 Determination of tip-sample interactions with an SPM in Dynamic Operation Mode

## 3.1 The free vibrating cantilever

The cantilever, excited to vibrations, is often described by the model of a beam fixed on one side [7], [9], [50], [55] and [56]. In case that no interaction forces are arising between the cantilever and the sample this system can be expressed by the equation of motion of a disturbed harmonic oscillator which is given as

$$m\ddot{z} + \gamma\dot{z} + kz = F_0 \cos(\omega t) . \quad (3.1)$$

In this model  $m$  is the effective mass, consisting of the distributed cantilever mass and the concentrated mass of the tip,  $\gamma$  a coefficient describing the damping properties of the system and  $k$  the spring constant of the cantilever. The term on the right side of Eq. 3.1 is the excitation force.

### 3 Determination of tip-sample interactions

---

Under some conditions, especially when higher orders of vibrations have to be taken into account, this model is too simple and more complicated approaches have to be used for an appropriate description [57], but as the cantilevers are operated in the range of their fundamental resonance frequency in the present work, this issue will be neglected in the following.

The damping coefficient  $\gamma$  in Eq. 3.1 can be expressed as

$$\gamma = \frac{m\omega_0}{Q} = \frac{k}{Q\omega_0}, \quad (3.2)$$

introducing the quality factor of the cantilever in this description. The quality factor  $Q$  determines the *broadness* of the magnitude peak and is defined as

$$Q = \frac{\omega_0}{\Delta\omega_{3dB}}, \quad (3.3)$$

where  $\Delta\omega_{3dB}$  is the so-called *3dB-bandwidth* of the system. Solving this equation leads to the well-known Lorentz profile given as

$$A(\omega) = \frac{A_0}{\sqrt{(\omega_0^2 - \omega^2)^2 + \left(\frac{\omega_0 \omega}{Q}\right)^2}} \quad (3.4)$$

for the frequency response of the magnitude and to

$$\varphi(\omega) = \arctan\left(\frac{\omega_0 \omega}{Q(\omega_0^2 - \omega^2)}\right) \quad (3.5)$$

for the frequency response of the phase between the driving force and the response measured by the PSD [39].

### 3.1 The free vibrating cantilever

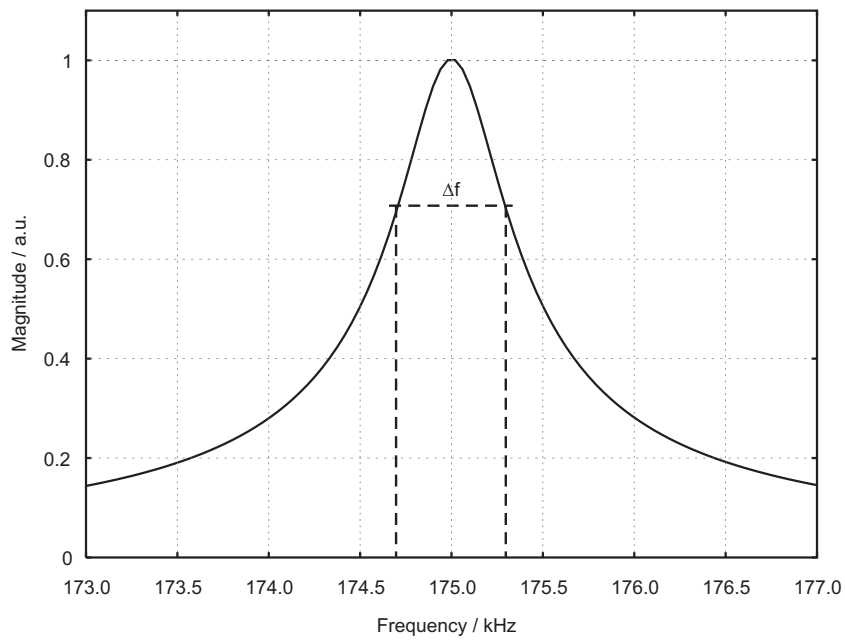


Figure 3.1: Amplitude response of the driven cantilever

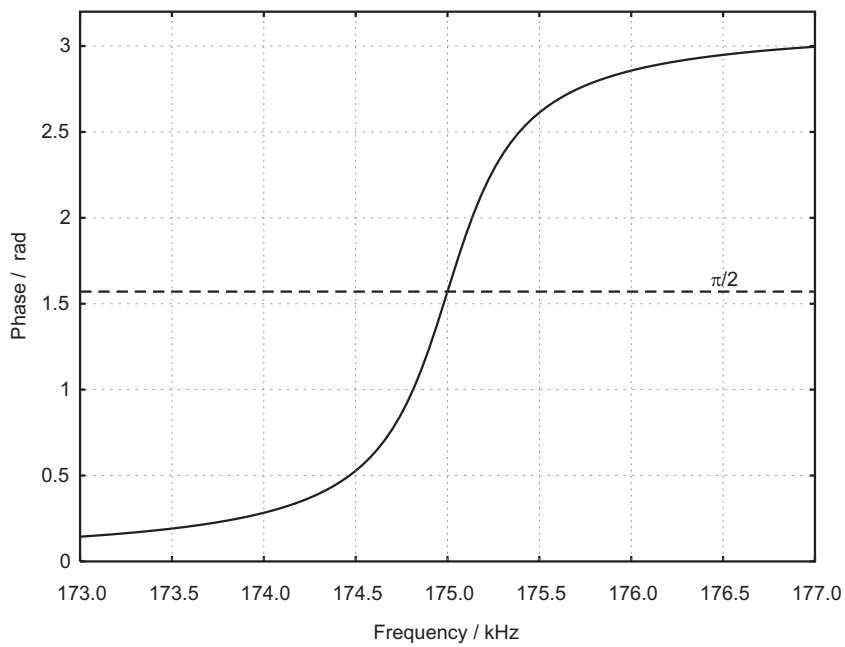


Figure 3.2: Phase response of the driven cantilever

Fig. 3.1 and 3.2 show plots of these response functions for a typical cantilever with a resonance frequency of  $f_0 = 175kHz$  and a quality factor of  $Q = 300$  in air. As clearly visible in the amplitude plot, the system is in resonant mode at its eigenfrequency  $f_0$ , reaching maximum amplitude and a phase value of  $\pi/2$ .

Tip-sample interactions will force a change of this behavior leading to a shift of the resonance frequency and to a reduced magnitude (see Sec. 3.3). As these changes are dependent on the mean distance between tip and sample, both effects are used for distance control in dynamic mode SFM imaging.

## 3.2 Distance control in dynamic mode microscopy

### 3.2.1 Slope detection

The slope detection scheme for the regulation of the mean distance between tip and sample was introduced in 1986 by [6] originally for the detection of magnetic fields by the use of the magnetic force microscopy. In this mode, the cantilever is excited to vibrations at a constant frequency  $\omega_d$  near to its resonance frequency  $\omega_0$ . The present oscillation amplitude at  $\omega_d$  is detected. A change of the mean distance between tip and sample leads to a shift of the resonance frequency of the cantilever, which causes also a change of the detected amplitude at the frequency  $\omega_d$ . The amplitude is fed to a control loop, which regulates by adjusting the piezo voltage of the z-piezo the mean tip-sample

distance in such a manner that the detected oscillation amplitude remains constant.

The slope detection scheme is now widely implemented in many self designed and commercial available instruments. Most of these instruments are operating in the attractive force regime, relatively far-away from the sample, to avoid stability problems of the feedback loop due to the non-monotonic properties of the force curve (see Sec. 2.6). For low vibration amplitudes ( $z_0 \ll Z$ ) the tip is not *touching* the surface and the mode thus is often referred to as non-contact operation mode, while for big vibrations amplitudes, when the tip *touches* the surface, the terms tapping mode or intermittent contact mode are often used. To achieve high sensitivity in slope detection, a steep slope of the cantilever frequency response is necessary. This can be obtained by increasing the quality factor  $Q$ , which can be easily done e.g. by operating the cantilever at low ambient pressure. Unfortunately the response time  $\tau$  of the cantilever is also increasing with the quality factor as given by

$$\tau = \frac{2Q}{\omega_0} \quad (3.6)$$

limiting thus the possible measurement bandwidth [7].

#### 3.2.2 Frequency modulation detection

Preservation of the measurement bandwidth, despite an increase of the quality factor, is achieved by the use of the frequency modulation (FM) detection scheme. FM detection was originally introduced in 1990 for Magnetic Force Microscopy (MFM) [7]. In this detection scheme the vibrating cantilever acts as the frequency-determining

component of an oscillator. The oscillator feedback loop locks the cantilever to its *natural resonance frequency*, which is also determined by the applied force gradient. On a change of this force gradient the resonance frequency of the oscillator will be changed immediately, not restricted by a response time like in slope detection. An appropriate FM demodulator, e.g. a PLL circuit locked on the cantilever resonance frequency, detects the frequency change and provides the feedback controller with an appropriate signal for the regulation of the mean tip-sample distance. FM detection is not as common as slope detection particular not in commercial available instruments. Nevertheless, impressive results have been achieved with this technique. Recent publications suggest that subatomic resolution is achievable using this technique, especially in combination with very low vibration amplitudes [52], [60].

### 3.3 Influences of tip-sample interactions on the vibrating cantilever

Arising forces due to tip-samples interactions, can still handled by the harmonic oscillator model in case of low energy dissipation of the cantilever vibration. The interaction can then be taken into account by introducing an additional term  $F_{TS}$ , describing the tip-sample forces. The modified equation of motion is given by

$$m\ddot{z} + \gamma\dot{z} + kz = F_0 \cos(\omega t) + F_{TS} . \quad (3.7)$$

A general solution of Eq. 3.7 is not obtainable as  $F_{TS}$  is dependent of

the specific structure of the tip and the sample. If the chemical structure of the tip and the sample is well-known an appropriate interaction function  $F_{TS}$ , based on the fundamental interaction mechanisms presented in Chapter 2, may be modelled, and the exact solution for this specific case can be calculated using numerical methods. Manifold methods based on classical and molecular dynamic approaches have been developed for this purpose, e.g. [48], [49] and [51].

In *real-world* experiments however, especially if unpure or even unknown samples shall be investigated, finding an appropriate functional description for the the tip-sample interactions becomes very difficult. Theoretical treatment in such cases can be enabled by using simplified functions and fitting experimental obtained data for the determination of the parameter [9]. Generalized potential functions, like the Lennard-Jones potential presented already in section 2 also simplify the modeling of tip-sample interactions. Further simplification can be achieved under consideration of the experimental operation conditions.

## 3.4 Determination of tip-sample interactions using a force based approach

One often used assumption [7], [55], [50], is the small amplitude approximation considering an interaction force  $F_{TS}$  arising from the Lennard-Jones potential. For a vibration amplitude  $A$  of the cantilever smaller than the mean tip-sample distance  $Z$ , as shown in Fig. 3.3, the force

### 3 Determination of tip-sample interactions

profile may be approximated by a first order function given by

$$F'_{TS}(Z + z(t)) = F(Z) + \frac{\partial F}{\partial z}(Z)z(t), \quad (3.8)$$

where  $z(t)$  is describes the vibration around this position.

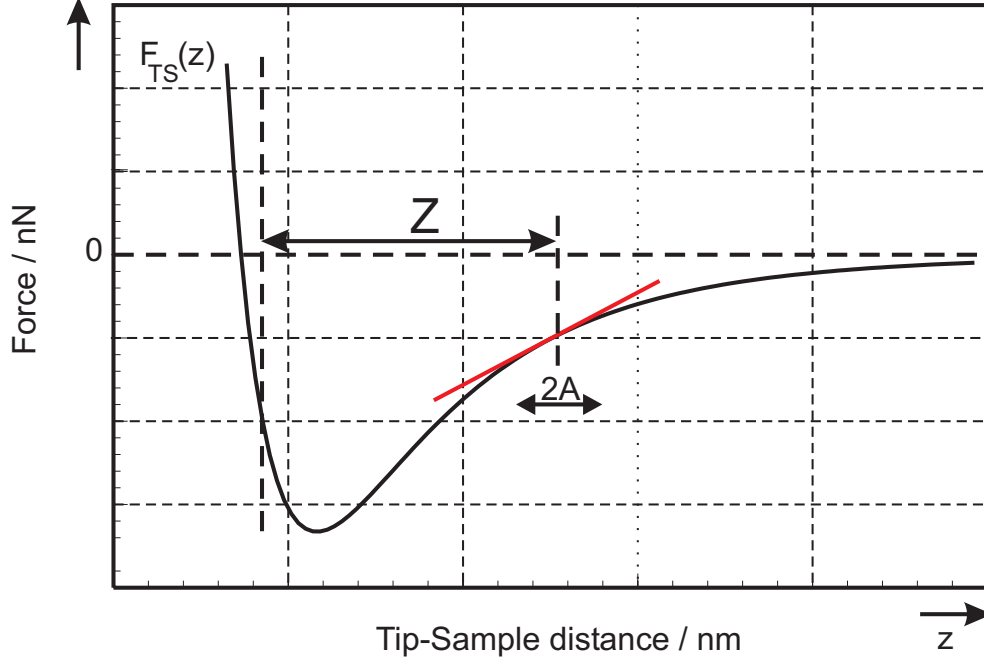


Figure 3.3: Tip-sample interactions for small vibration amplitudes

The equation of motion can be written in this case as

$$m\ddot{z} + \gamma\dot{z} + kz = F_0 \cos(\omega t) + F(Z) + \frac{\partial F}{\partial z}(Z)z(t). \quad (3.9)$$

Considering the force gradient as a *sample spring constant* and summing it with the cantilever's own spring constant to an effective force constant given by

$$k_{eff}(Z) = k - \frac{\partial F}{\partial z}(Z). \quad (3.10)$$

Eq. 3.9 can be solved in analogy to Eq. 3.1 leading to

$$A(\omega, Z) = \frac{A_0}{\sqrt{(\omega'_0(dF/dz, Z)^2 - \omega^2)^2 + \left(\frac{\omega'_0(dF/dz, Z) \omega}{Q'(dF/dz, Z)}\right)^2}} \quad (3.11)$$

for the magnitude and for the phase to

$$\varphi(\omega, Z) = \arctan \left( \frac{\omega'_0(dF/dz, Z) \omega}{Q'(dF/dz, Z)(\omega'_0(dF/dz, Z)^2 - \omega^2)} \right). \quad (3.12)$$

The resonance frequency and the quality factor are dependent on the force gradient, which is dependent on the mean tip-sample distance, and given as

$$\omega'_0(dF/dz, Z) = \omega_0 \sqrt{1 - \frac{1}{k} \frac{\partial F}{\partial z}(Z)} \quad (3.13)$$

and

$$Q'(dF/dz, Z) = Q \frac{\omega'_0(Z)}{\omega_0}. \quad (3.14)$$

If all other parameters are known, the force gradient can thus be determined by measuring the resonance frequency or the quality factor of the cantilever.

### 3.5 Determination of tip-sample interactions using an energy based approach

Another interesting approach for the determination of tip-sample interactions in force microscopy is the consideration of the energy flow in the system as proposed in [58] and [59].

In equilibrium state the dissipated energy can be expressed as

$$\overline{P_{in}} = \overline{P_0} + \overline{P_{Tip}}, \quad (3.15)$$

### 3 Determination of tip-sample interactions

---

where  $\overline{P_{in}}$  is the average energy fed into the vibrating system,  $\overline{P_0}$  is regarded as *background* dissipation caused by the cantilever damping, e.g. through air damping, and  $\overline{P_{Tip}}$  the energy dissipated due to tip-sample interactions.

The input power for a sinusoidally driven cantilever, with driving amplitude  $A_d$ , can be expressed as

$$\overline{P_{in}} = \int_0^T P_{in}(t) dt = \frac{1}{2} k A_d A \omega \sin(\varphi) , \quad (3.16)$$

with  $k$  as the force constant,  $A$  the vibration amplitude and  $\omega$  the vibration frequency of the cantilever and  $\varphi$  as the phase shift between the driving signal and the cantilever response.

The background dissipation can be expressed similarly using the damping coefficient  $\gamma$  as

$$\overline{P_0} = \frac{1}{2} \gamma A^2 \omega^2 . \quad (3.17)$$

Using these equations and the relationship for  $\gamma$  given in Eq. 3.2, the dissipated energy due to tip-sample interactions can be calculated as

$$\overline{P_{Tip}} = \overline{P_{in}} - \overline{P_0} = \frac{1}{2} \frac{k\omega}{Q} \left( Q A_d A \sin(\varphi) - A^2 \frac{\omega}{\omega_0} \right) \quad (3.18)$$

For  $\omega = \omega_0$  this equation can be simplified using the relationship of the free oscillation amplitude  $A_0 = Q \cdot A_d$  to

$$\overline{P_{Tip}} = \frac{1}{2} \frac{k\omega}{Q} \left( A_0 A \sin(\varphi) - A^2 \right) \quad (3.19)$$

An appropriate frequency analysis system, with the ability to measure the amplitude and the phase shift of the vibrating cantilever simultaneously, can thus determine the tip-sample dissipation energy immediately.

### 3.6 Determination of polymer properties with dynamic mode SPM

A main application field for the realized system is the microscopic investigation of thermomechanical properties of polymers. Standard methods for polymer characterization, like the Differential Scanning Calorimetry (DSC), Dynamic Mechanic (Thermal) Analyzer (DMTA) or Dielectric Analyzer (DEA), are used for a macroscopic determination of the above given parameters as they are measuring integrally over a bulk volume [70]-[74].

With the increasing interest in the analysis of the microscopic structure of polymers several methods have been developed which make use of scanning probe techniques. So far developed methods like e.g. Scanning Friction Force Microscopy (SFFM) or Micro Thermo Analysis ( $\mu$ TMA) make advantage of the high resolution of the SPM but destroy the sample during investigation as they apply a destroying force on the surface [75], [20], [13], [19]. The here presented method works contact less and thus non-destructive.

As known from standard literature of polymer sciences, for temperatures below  $T_G$  the chain mobility of polymers is frozen [70]. The whole material is behaving like a rigid spring, storing energy fed into the polymer as potential energy. A static microscopic behavior of the polymer chains is thus expected. In the attractive region, the SPM tip will sense van der Waals forces, which are mainly determined by the tip-sample distance.

If the temperature increases above  $T_G$  the chain mobility increases

### *3 Determination of tip-sample interactions*

---

and the material is in a state similar to rubber. According to chapter 2, this process is linked to the rotation of the different dipoles forming the polymer chain. The polymer chains can flow, as various energetic equal states are possible, changing thus the volume and the spring constant of the material.

As long as the dipoles are rotating within the chain and the chain does not break, this process is only a function of the molecular movement and thus reversible. The vibrating tip above the polymer will sense therefore a different force gradient in dependency of the temperature which is used to create a local temperature profile, without destroying the sample.

Further increase of the temperature will change the elasticity properties of the polymer further and will lead, especially above the melting temperature  $T_M$ , to a behavior of the polymer comparable to viscous fluids, destroying finally the polymer structure.

# 4 The Scanning Probe Microscope

Investigation of the local thermomechanical properties of materials can be performed, as presented in the previous section, by probing the intermolecular force gradients between the tip and sample in dynamic operation mode. Using a commercially available SPM instrument for this purpose, the properties of the instrument have to be known for correct interpretation of the acquired data. A brief general overview of the properties of the used instrument is thus presented in this section.

## 4.1 Experimental Setup

The fundamentals of design, instrumentation, and applications of Scanning Probes Microscopes are described in detail in many published works. Especially [23] and [24] give a good comprehensive overview. The experimental setup for the detection of intermolecular forces is used as shown in Fig. 4.1.

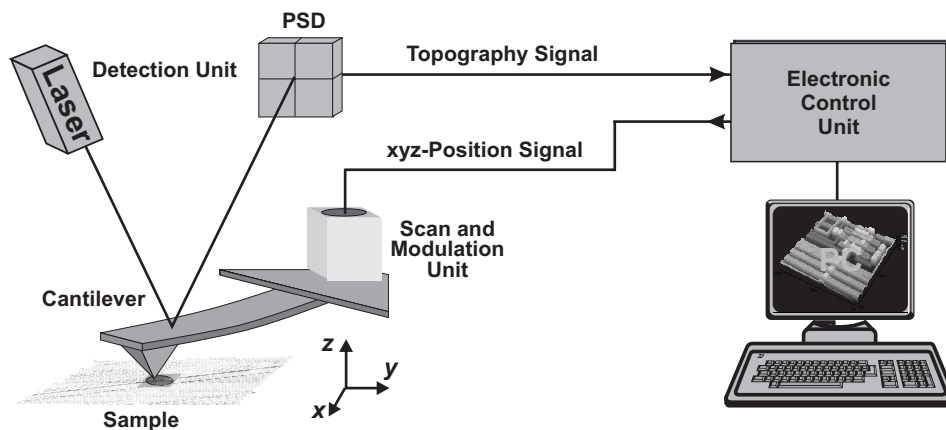


Figure 4.1: Principle Setup of a Scanning Probe Microscope

The heart of the SPM is the force probe, a needle-sharp tip attached to the very end of a cantilever. The cantilever is fixed on the other side on a base which can be moved<sup>1</sup> in any spatial direction by piezoelectric actuators with very high resolution. Forces are measured indirectly by detecting the bending of the cantilever. Different detection schemes have been developed for this in the past years. In the first SPM a tunnelling current detection circuit was used as a legacy to the former developed STM and measured the cantilever bending by adjusting a tunnelling tip in close proximity over the cantilever [3]. Nowadays, especially for commercial available SPM, force measurement using optical deflection methods is a widely spread used technique [23].

A computer controlled electronic control unit (ECU) applies voltage signals to the xy-piezo-actuators in an appropriate way so that the tip scans over a rectangular area of the surface. Typical scan ranges are between  $1\mu m$  and  $100\mu m$ , depending on the type of the scanner. The

---

<sup>1</sup>There exist different realizations of Scanning Probe Microscopes. In some of them the probe is scanned, in others the scanner moves the sample.

cantilever's bending is transformed via the optical detection circuit into an electrical signal and can be used directly, according to Eq. 2.1, to form the image. This so called *constant height mode* is not used very frequently, as, depending on the surface profile, very high forces can occur which can destroy the tip, the cantilever and the sample. It is more common to operate the SPM in the so called *constant force mode*. In this mode any bending of the cantilever is fed to a PID controller. The control loop adjusts the voltage on the z-piezo in such a manner that a given bending (and thus force) will be maintained. The output of the PID controller is used in this mode to form the image.

Stress and strain between tip and sample can be minimized by the control loop, but a principal residual force in both of these *contact modes* is unavailable. For many samples, especially soft ones like biological tissues or polymers, this is not tolerable. Applying virtually no force between tip and cantilever is one main advantage of the so called *dynamic operation mode* (see section 3).

## 4.2 The Force Probe

Standard force probes for resolving surface topography are characterized by their geometrical and mechanical properties. For a noncontact-mode probe made of silicon as shown in Fig. 4.2 typical geometric dimensions as given in the datasheets are shown in the following table [26].

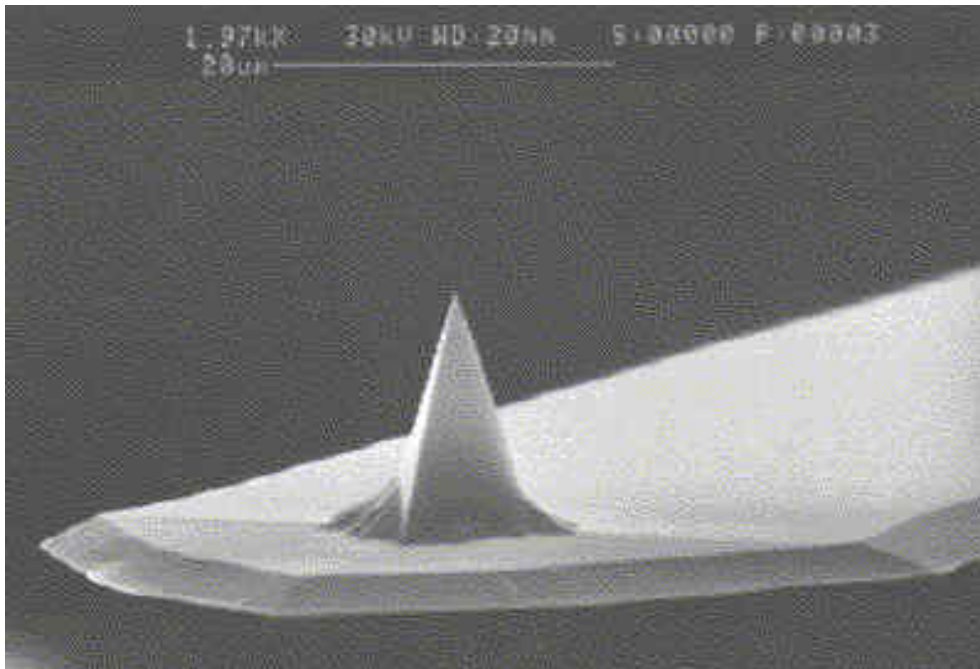


Figure 4.2: SEM image of a Force Probe [26]

Technical Data	Contact Mode	Non-Contact Mode
Length:	445 $\mu m$	125 $\mu m$
Mean Width:	50 $\mu m$	30 $\mu m$
Thickness:	2 $\mu m$	4 $\mu m$
Force Constant:	0.2 $N/m$	42 $N/m$
Resonance Frequency:	13 $kHz$	330 $kHz$

Table 4.1: Typical technical data of a Scanning Probe Cantilever

The tip height itself is about 15  $\mu m$  with a macroscopic cone angle of about 50°. Knowing the shape and exact dimensions of a cantilever allows the theoretical determination of the most important mechanical parameters, the force constant  $k$  and the resonance frequency  $\omega_0$ .

As derived from [23], the force constant for a rectangular shaped cantilever can be calculated as

$$k = 3 \frac{EI}{L^3}, \quad (4.1)$$

where  $E$  is the Young' modulus<sup>2</sup>,  $I$  the area moment of inertia, which is dependent on the cantilever's shape and dimensions, and  $L$  the length of the cantilever.

Knowing the dimensions,  $T$  is the thickness and  $L$  the length of the cantilever, and the material density<sup>3</sup>  $\rho$  the resonance frequency<sup>4</sup> can be calculated [25] using

$$f_0 = 0.162 \cdot \sqrt{\frac{E}{\rho}} \cdot \frac{T}{L^2}. \quad (4.2)$$

As the dimensions of every cantilever differ a little bit, theoretical calculation based on the above given typical values can be used only as a first approximation. If the exact values for the force constant and resonance frequency are required, the exact dimensions of every individual cantilever must be determined experimentally. Different calibration methods have been developed for this purpose [30]-[33].

Force probes have become a standard tool in nanotechnology in the past years and are today commercially available in a great variety of types with different properties. Nevertheless it is sometimes still necessary to modify existing tips or to develop new tip designs to fulfill special requirements. For Scanning Thermal Microscopy e.g. a thermal sensitive tip is required. Existing tips for this specific SPM-branch still don't allow the achievement of optimum performance.

<sup>2</sup> $E = 98GN/m^2$  for silicon [28]

<sup>3</sup> $\rho = 2330kg/m^3$  for silicon [25], [29]

<sup>4</sup>In this formula the mass of the tip is neglected

New designs combining high spatial resolution with high thermal resolution are therefore desirable [17]. Other requirements come from the biomedical application field. In this field, work is performed to measure interaction forces between different cells and tissues, e.g. to test the compatibility of prostheses. For this kind of applications biological and chemical sensitive tips are required. As there are no standardized probes for these very specific purposes, commercial probes are modified to fulfill these requirements [27]. As it is expected that the use of specialized probes will increase rapidly in future, it is very important that the instrument's designers provide the ability to use a great variety of different kind of probes. One critical component which can limit this ability is the implemented type of detection system.

### 4.3 Detection Unit

#### 4.3.1 Optical Deflection Detection

For commercially available SPM, like the *Topometrix TMX 2000 Explorer System*, which was used for the present work, the deflection detection system has become the dominant measuring system for force detection. Optical deflection detection has a lot of advantages compared to other methods. It is quite sensitive, relative easy to handle and can operate under different ambient conditions. As any part of the optical detection system is quite far away from the probe, a destruction of the probe, e.g. through a *tip crash*, will not affect the detection system [23]. Unlike e.g. the piezoelectric detection scheme, optical deflection is widely independent from the chosen type of the

force probe. The deflection system, as shown in Fig. 4.3, consists of a laser source, which is focused on the cantilever by a lens, and a position sensitive detector, often realized using four<sup>5</sup> photo diodes (PD) arranged in matrix form, to measure the reflected light.

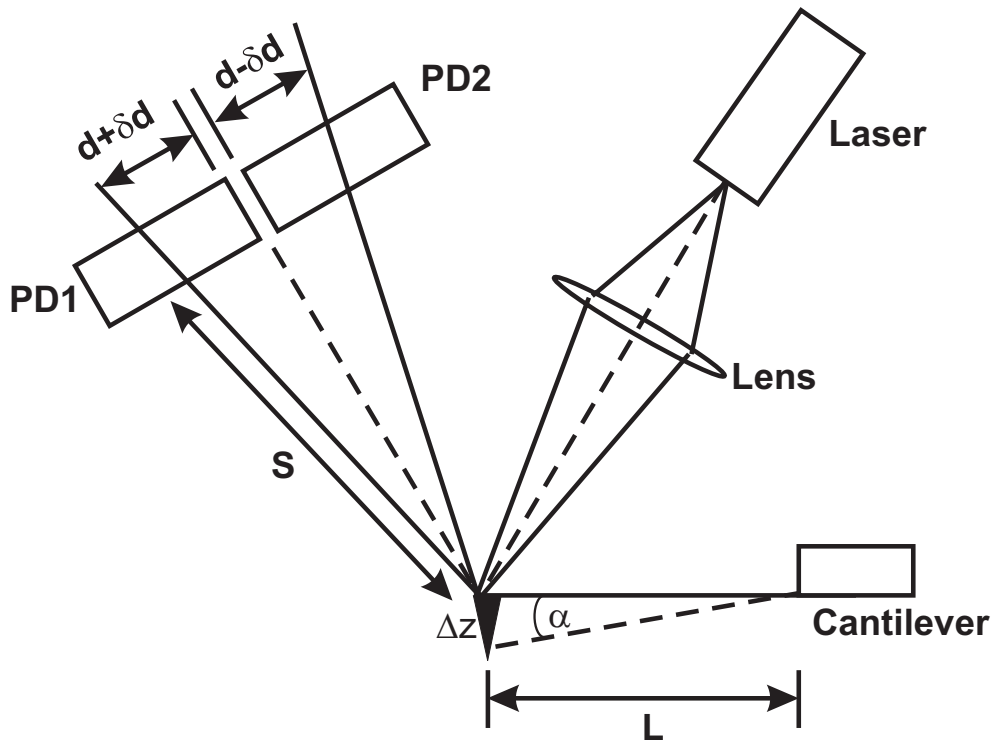


Figure 4.3: Optical Deflection Detection System

In presence of a force  $F$  the cantilever will be bended at its end by an angle of

$$\alpha = \frac{FL^2}{2EI} \quad (4.3)$$

With

$$EI = \frac{kL^3}{3} \quad (4.4)$$

<sup>5</sup>In fig. 4.3 only two of them, PD1 and PD2, are shown for simplicity

and

$$F = k \cdot \Delta z \quad (4.5)$$

the bending angle can be expressed as

$$\alpha = \frac{3}{2} \frac{\Delta z}{L}, \quad (4.6)$$

producing a linear deflection  $z$  for a given angle  $\alpha$  [23]. Applying fundamental geometric considerations, it is clearly visible that the deflection  $z$  of the cantilever is transformed to a deflection in the photodetector plane  $\delta d$  given by

$$\delta d = 3 \frac{S}{L} \Delta z = \beta \Delta z \quad . \quad (4.7)$$

The term  $\beta$  is known as *optical amplification*. For typical cantilever lengths of  $L = 300 \mu m$  and typical cantilever-detector distances of  $S = 3 cm$  the optical amplification factor  $\beta$  is typically about 300. This amplification can not be magnified arbitrarily simply by increasing the distance between the cantilever and the photodetector, as increasing distances lead to a stronger defocusing of the laser beam and therefore to a loss in sensitivity.

### 4.3.2 Photodetector and Instrumentation

The conversion of the linear motion of reflected laser light into an equivalent electric signal is done by the *Position Sensitive Detector* (PSD). These detectors can be realized as non-discrete position sensors, utilizing photodiode surface resistance [34] or, which is claimed to be more sensitive, by arranging individual photodiodes in a matrix and measuring the differential value of the photocurrents generated

by incident radiation [36]. As the latter principle is implemented for opto-electrical conversion in the SPM used in this work, the properties of the *Four Quadrant Detector* shall be presented briefly in the following as derived from [37]-[39].

### Four Quadrant Detector

Position sensitive detectors based on quadrant silicon photodiode devices are realized by arranging four active Si-photodiodes as shown in Fig 4.4 [36]. Every anode is bonded individually to a device pin, but the PSD uses a common cathode which is also connected with the device's case. The dimensions of each quadrant are about  $1.23\text{ mm} \times 1.23\text{ mm}$ , forming an active area of about  $1.5\text{ mm}^2$ , and separated from each other at a distance of about  $0.05\text{ mm}$ .

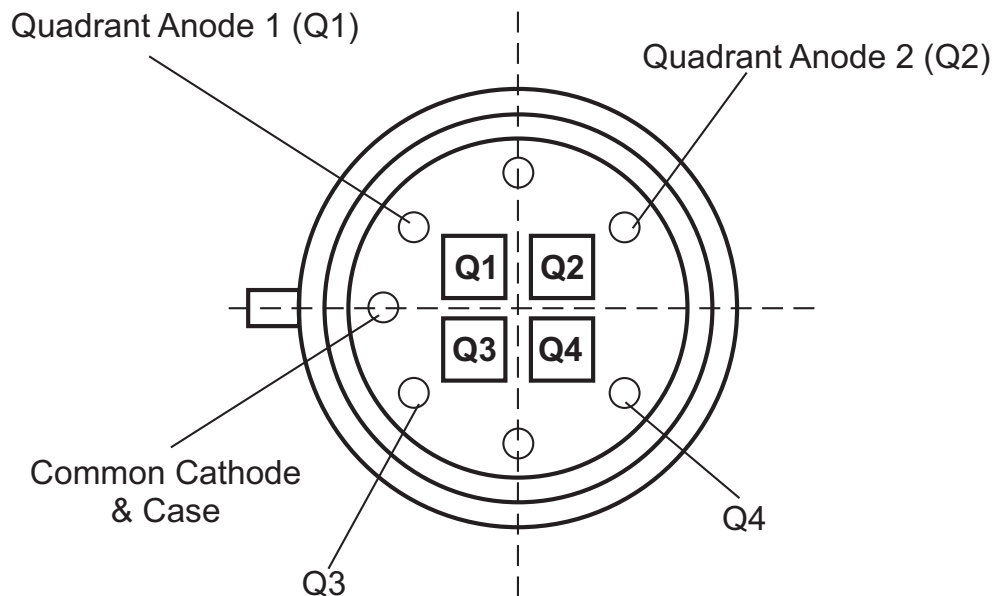


Figure 4.4: Schematic setup of a quadrant silicon photodiode

Every photodiode is realized by a pn-junction, using a high purity n-doped silicon bulk material and a very thin p-doped layer forming the active region. Fig. 4.5 shows the principle cross section of such a photodiode [37].

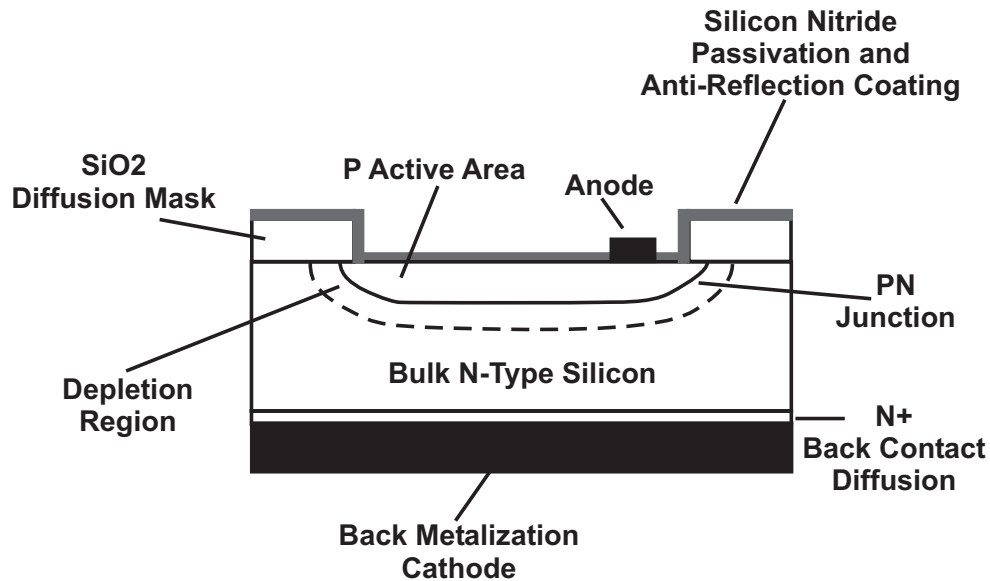


Figure 4.5: Schematic cross section of a pn-photodiode

The active area is coated with a passivation material, often silicon nitride, which protects the semiconductor and serves also as an anti-reflection coating. The thickness of this coating as well as the thickness of the p-doped region are optimized for the specific wavelength to be detected. The depth of the depletion region which is generated at the pn-junction can be varied by applying a reverse bias voltage across the junction, influencing also the capacitance of the pn-junction. According to the *Photovoltaic Effect*, incident radiation creates electron-hole pairs, which cause a current  $I_L$ .

### Photodiode Responsivity

The amount of current generated is dependent on the *Photodiode Responsivity*, which is the ratio of the photocurrent output to the radiant energy incident on the photodiode and given in A/W.

$$R = \frac{I_L}{P} \quad (4.8)$$

The responsivity depends on the wavelength of the incident radiation and the applied bias voltage. A typical value for the responsivity is about  $R = 0.5 \text{ A/W}$  for the usually used red LED-laser with  $\lambda = 640 \text{ nm}$  and a reverse bias voltage of  $U_B = 10 \text{ V}$  [36].

### Equivalent Circuit

Photodiodes can be regarded as current sources and described using the following equivalent circuit,

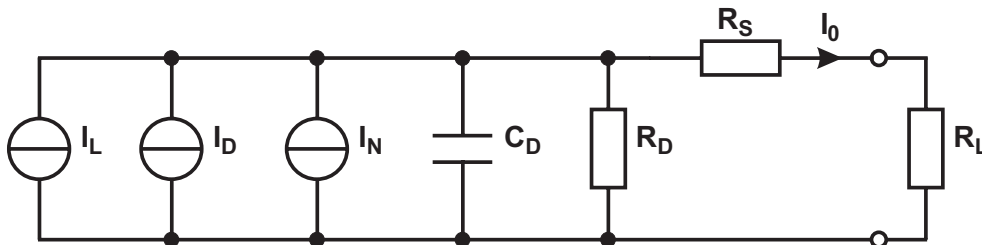


Figure 4.6: Equivalent electrical circuit of a Si-photodiode

where  $I_L$  is the light current generated by the radiation,  $I_D$  a leakage or *dark* current source, generated by the applied bias voltage.  $I_N$  represents the noise which is generated in the device.  $C_D$  is the bias voltage dependent junction capacity,  $R_D$  the parallel shunt resistance,  $R_S$  the diode's series resistance and  $R_L$  the load resistance.

### Noise considerations

The noise current is formed mainly by *Shot Noise* current, resulting from the light and the dark current, and a *Johnson Noise*, due to the resistance of the device. The total noise current can be calculated as the root mean square sum of the individual noise current contribution:

$$I_N = \sqrt{I_{Johnson}^2 + I_{Shot,D}^2 + I_{Shot,L}^2} \quad (4.9)$$

The shot noise can be calculated using

$$I_{Shot,L} = \sqrt{2 e I_L B} \quad (4.10)$$

and

$$I_{Shot,D} = \sqrt{2 e I_D B} , \quad (4.11)$$

the Johnson noise using

$$I_{Johnson} = \sqrt{\frac{4 k T B}{R}} \quad (4.12)$$

where  $e$  is the electronic charge<sup>6</sup>,  $k$  Boltzman's constant<sup>7</sup>,  $T$  the absolute temperature,  $B$  the measurement bandwidth and  $R$  the effective resistance.

In normal operation the shot noise contribution from the light current will be predominant, as the shot noise for a typical light current of  $I_L = 50\mu A$  will be approximately  $I_{Shot,L} = 4pA$  at a bandwidth  $B = 1Hz$ , but if the minimum detectable light shall be estimated, the other noise contributions have to be regarded as well. For non-biased

---

<sup>6</sup> $e = 1.6 \cdot 10^{-19} As$

<sup>7</sup> $k = 1.38 \cdot 10^{-23} J/K$

operation the Johnson Noise dominates in this case, as the dark current is approaching zero, but for the most common reversed bias operation mode, the dark shot noise gives the dominant contribution. For a typical given dark current of  $I_D = 1 \text{ nA}$  at  $U_B = 10\text{V}$  at a bandwidth of  $B = 1\text{Hz}$  the Shot Noise is  $I_{Shot,D} = 17,9\text{fA}$  while the Johnson Noise is only about  $I_{Johnson} = 5,7\text{fA}$  assuming an effective shunt resistor of  $R_{Shunt} = 500 \text{ M}\Omega$  [35], [36].

### Dynamic Performance

The response time of a photodiode is the root mean square sum of the charge collection time  $T_{CC}$  and the RC time constant  $\tau$ , arising from the involved resistors<sup>8</sup> and capacitances<sup>9</sup>.

$$T_R = \sqrt{T_{CC}^2 + \tau^2} \quad (4.13)$$

The charge collection time depends on the bias voltage and consists of a fast and a slow component. Electron-hole pairs, generated by incident radiation are separated by two different effects. By the diffusion process, which is relative slow, and by the existing electric field, due to the applied bias voltage, which is the much faster effect. For unbiased operation, when diffusion is the dominant contribution, response times in the order of  $0.5 \mu\text{s}$  are achievable, while for a bias voltage of  $15 \text{ V}$ , response times in the order of  $100 \text{ ns}$  are given in the datasheets, going down to  $2 \text{ ns}$  depending on the wavelength.

<sup>8</sup>Series and load resistance.

<sup>9</sup>Mainly the junction capacity, but stray capacities play also an important role and should be minimized therefore for high dynamic performance.

For very short response times it is important to minimize stray capacitances as they can reduce response time significantly. The junction capacitance  $C_D$  is dependent on the bias voltage and given in the range between 25 pF and 10 pF, leading to a RC time constant of 10 ns<sup>10</sup> [36]. As this is already in the order of the charge collection time in biased operation mode, any additional stray capacitance will lead immediately to a decrease of dynamic performance.

### Instrumentation

The PSD built in the used SPM is operated in a non-biased photo-voltaic mode. Every photodiode is connected to an I/V-converter as shown in Fig. 4.7. As no bias voltage is applied, the dark current is minimal. The virtual ground at the input of the operation amplifier allows the operation of the photodiode to be independent from  $R_D$ . For an ideal system the conversion factor is given by  $R_k$  to

$$U_A = I_{PD} \cdot R_k , \quad (4.14)$$

but, as for the real sensor the junction capacity  $C_D$  can not be neglected, the transfer function of the I/V-converter<sup>11</sup> is given by

$$U_A = (I_{PD} + I_N) \cdot ((R_D || C_D) || (R_k || C_k)) + U_{OS} \cdot \left( 1 + \frac{R_k || C_k}{R_D || C_D} \right) , \quad (4.15)$$

where  $U_{OS}$  is the offset voltage of the operation amplifier and  $I_N$  is a current source describing the bias and offset currents of the operation amplifier [40].

---

<sup>10</sup>Calculation based on an effective R of 1 kΩ as given in the datasheet.

<sup>11</sup>Neglecting  $R_S$

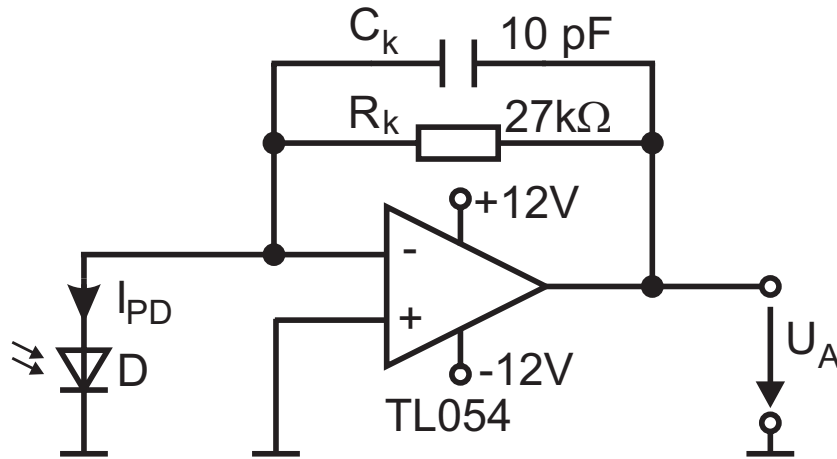


Figure 4.7: PSD Preamplifier

The sensitivity of the I/V-converter is directly determined by  $I_N$  and  $U_{OS}$ . For the TL054  $U_{OS} = 0.5mV$ ,  $I_B = 30pA$  and  $I_{OS} = 5pA$  are given as typical values [41]. The capacitor  $C_k$  preserves the stability of the feedback loop, while limiting the bandwidth of the converter. The full-scale output of the I/V-converter is defined to be  $\pm 10V$ , leading to a full-scale current of the photodiode of  $I_{PD,FS} \approx 400 \mu A$ . The 3 dB corner frequency is given to

$$f_{g,PSD} = \frac{1}{2\pi \cdot R_k C_k} \approx 590kHz . \quad (4.16)$$

This defines the absolute maximum measuring bandwidth of the whole SPM system.

Considering the noise properties of the given operation amplifier, the equivalent noise voltage density is given to  $e_n = 75 nV/\sqrt{Hz}$  at  $f = 10 Hz$  and to  $e_n = 21 nV/\sqrt{Hz}$  at  $f = 1 kHz$ , the equivalent current noise density is given to  $i_n = 0.01 pA/\sqrt{Hz}$  at  $f = 1 kHz$ , as typical values.

## 4.4 Modulation Unit

### 4.4.1 Piezo-Actuator

SPM-actuators are based on the piezo-effect, which is known since 1880 and was found first in natural occurring minerals by the Curie family. The piezo-effect, the occurrence of strain, which produces a mechanical displacement, on appliance of an electric field, is very small for natural piezoelectric materials. Industrial produced piezo-electric PZT-ceramics<sup>12</sup> however, which are especially designed in the present days for nanopositioning purposes, can produce displacements of up to 0.1 % of their length. Actuators, manufactured from such ceramics, use several PZT elements forming a stack as shown in Fig. 4.8.

As piezo stacks are electrically connected in parallel and mechanically in series, the individual displacement of each element is summed in this configuration, obtaining positioning ranges up to 100  $\mu m$  for a typical 100 mm long stack-actuator using relative low voltages. The use of mechanical amplification components can extend this range further [42]-[44].

---

<sup>12</sup>The term PZT is derived from the ceramics's main components: Pb, Zi, Ti.

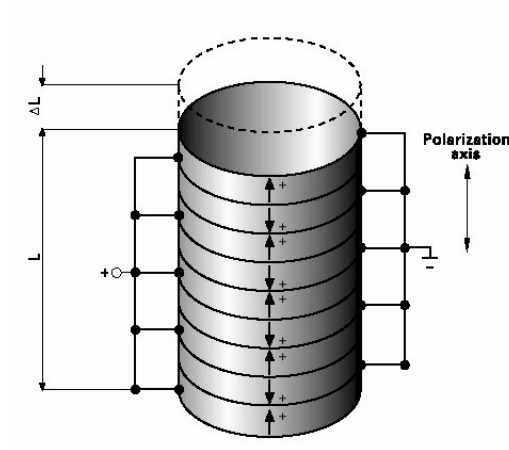


Figure 4.8: Schematic overview of a Piezo-Stack-Actuator [43]

The behavior of piezo-elements can be described using the linear piezo-electric state equations as defined in [44] and [45]. For the practical case of a piezo-actuator however, these equations can be simplified to

$$\Delta L \approx E \cdot d_{ij} \cdot L_0 . \quad (4.17)$$

In this equation,  $\Delta L$  is the piezo displacement,  $E$  the magnitude of the electrical field strength,  $L_0$  is the original length of the piezo actuator and  $d_{ij}$  the *piezoelectric coefficient* in  $ij$  direction.<sup>13</sup> The displacement direction and thus the value of  $d_{ij}$  depends on the actuator design. For stack actuators, where  $d_{33}$  is the relevant value, values between  $450$  and  $650 \cdot 10^{-12} \text{ m/V}$  are typical, while for tube actuators, where  $d_{31}$  is relevant, values between  $-200$  and  $-300 \cdot 10^{-12} \text{ m/V}$  are given. The maximum allowed field strength in poling direction is about 1 to

<sup>13</sup>The directions are defined corresponding to the common right-hand orthogonal axis-set, where X=1, Y=2, Z=3 and Z is the polarization direction.

2 kV/m [43]. For the used scanner, a nominal maximum operation voltage of 100 V is defined. The scanner generates at this voltage a displacement of about  $10\mu\text{m}$ .<sup>14</sup>

Due to the strong nonlinear response, large hysteresis and long term drift of piezoelectric actuators, the amount of displacement as a function of the voltage is not directly predictable and Eq. 4.17 can serve only as a coarse approximation. For appropriate excitation and detection of cantilever vibrations, it is therefore important to study the dynamic properties of the piezo-actuator. The dynamic mechanical behavior of piezo-actuators is determined by its effective mass  $m_{eff,PZT}$  and the stiffness  $k_{PZT}$  of the actuator. The mechanical system can be approximated by a second order system, with a mechanical resonance frequency as given by

$$f_{0,PZT,mech.} = \frac{1}{2\pi} \sqrt{\frac{k_{PZT}}{m_{eff,PZT}}}, \quad (4.18)$$

which is typically given in the datasheet of the actuator manufacturer [43].

The electrical behavior of the piezo-actuator can also be described as a second order oscillator, using the equivalent circuit diagram shown in Fig. 4.9 [44]. In this model  $R_r$  is determines the damping caused by piezo losses,  $L_r$  the mass of the actuator,  $C_r$  the elasticity and  $C_p$  the free capacitance. As  $C_p$  is much bigger than  $C_r$ , the piezo is considered often electrically as a capacitor defined by  $C_p$ .

---

<sup>14</sup>Dependent on the individual scanner

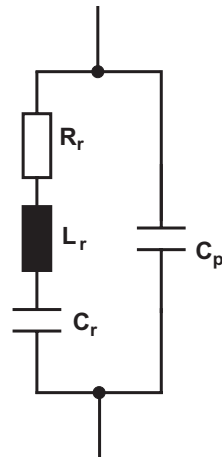


Figure 4.9: Electrical Equivalent Circuit of a Piezo-Actuator

#### 4.4.2 Signal Coupling

Beside the properties of the piezo-actuator, the overall properties of the modulation unit are influenced also by the modulation coupling instrumentation. In normal imaging mode a voltage up to 100 V is applied by the Topography-Feedback-Controller of the ECU onto the piezo. To avoid interference of this voltage with the modulation signal, an appropriate signal coupling mechanism must be provided. This coupling mechanism is realized as shown in Fig. 4.10.

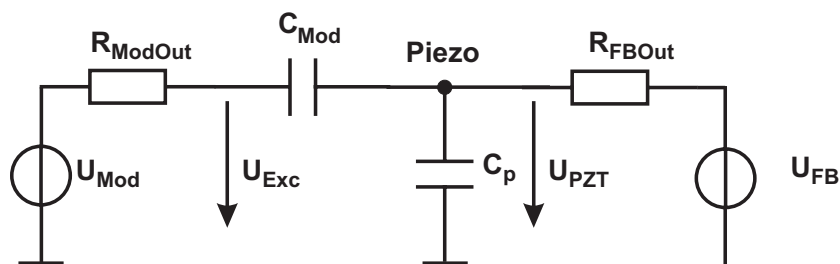


Figure 4.10: Signal Coupling for Modulation Input

The piezo-actuator is represented in this figure only by its parallel capacitance  $C_p$ . The amplifier of the ECU feedback-loop is described by the voltage source  $U_{FB}$  and the serial resistor  $R_{FB,Out}$ . The modulation source is also characterized by a voltage source,  $U_{Mod}$  and a serial resistor  $R_{Mod,Out}$ , coupled by the capacitor  $C_{Mod}$  to the piezo.

In absence of a feedback voltage  $U_{FB}$ , the transfer function for  $U_{Mod}$  is given as

$$\frac{U_{PZT}}{U_{Mod}} = \frac{1/\alpha}{1 + j\omega \frac{R_{Mod,Out}C_p}{\alpha} + \frac{1}{j\omega\alpha R_{FB,Out}C_{Mod}}} \quad (4.19)$$

with

$$\alpha = 1 + \frac{C_p}{C_{Mod}} + \frac{R_{Mod,Out}}{R_{FB,Out}}. \quad (4.20)$$

For low frequencies  $R_{Mod,Out}$  and  $C_p$  can be neglected, and the transfer function is dominated by the RC high pass formed by  $C_{Mod}$  and  $R_{FB,Out}$  with a high pass corner frequency given by

$$f_{g,HP} = \frac{1}{2\pi\alpha R_{FB,Out}C_{Mod}}, \quad (4.21)$$

while for high frequencies  $C_{Mod}$  and  $R_{FB,Out}$  can be neglected, leading to a dominating low pass behavior given by  $R_{Mod,Out}$  and  $C_p$  with a low pass corner frequency given by

$$f_{g,LP} = \frac{1}{2\pi\alpha R_{Mod,Out}C_p}. \quad (4.22)$$

The frequency response of  $U_{PZT}$  and  $U_{Exc}$  is simulated and shown in Fig. 4.11 in comparison to  $U_{Exc}$ , measured at the SPM.

The deviations between the simulated and the measured response of the excitation voltage  $U_{Exc}$  are expected to be caused by resonance effects of the piezo-actuator and different mechanical parts of the instrument, which are neglected in the simulation. The piezo voltage

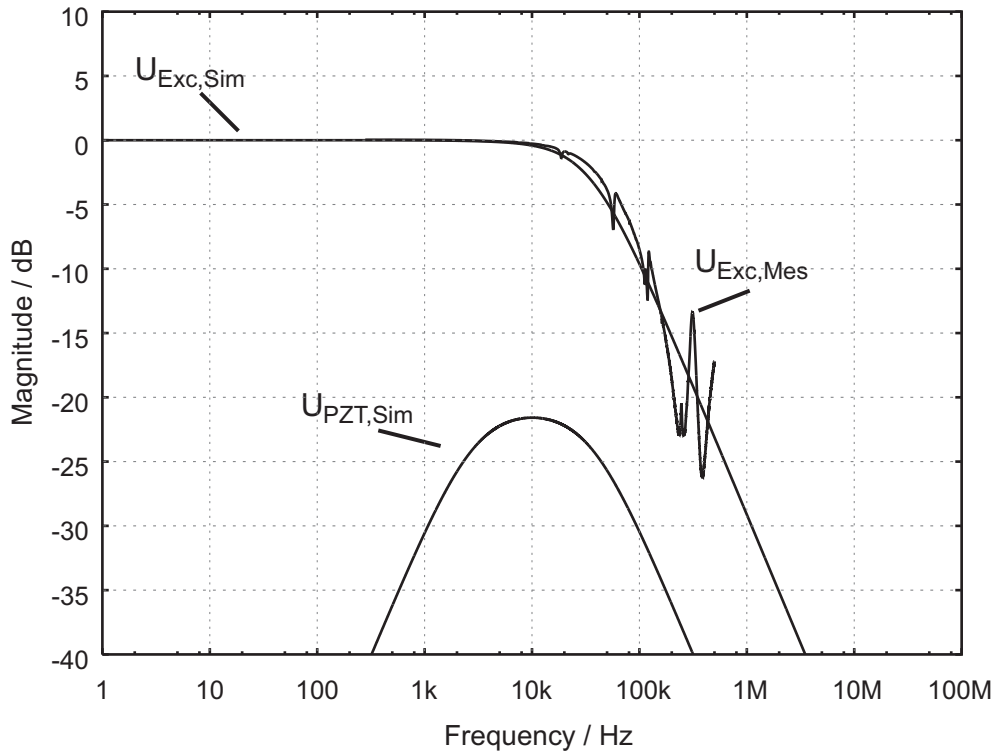


Figure 4.11: Simulated excitation and piezo voltage in comparison to the measured excitation voltage

will therefore deviate also from the simulated curve in Fig. 4.11 exciting mechanical vibrations. The vibrations are observable if the electrical signal is compared with the mechanical measured by the PSD. Fig. 4.12 shows the linearly scaled frequency response of  $U_{Exc}$  for two different excitation voltages, Fig. 4.13 the simultaneously acquired photo-detector-signal. It is clearly visible, that every distortion of the excitation voltage from the "ideal" simulated curve produces mechanical vibrations. The strong mechanical peak at 280 kHz in Fig. 4.13, which has no direct link to an electrical "distortion" is the cantilever resonance, as expected from cantilever's datasheet.

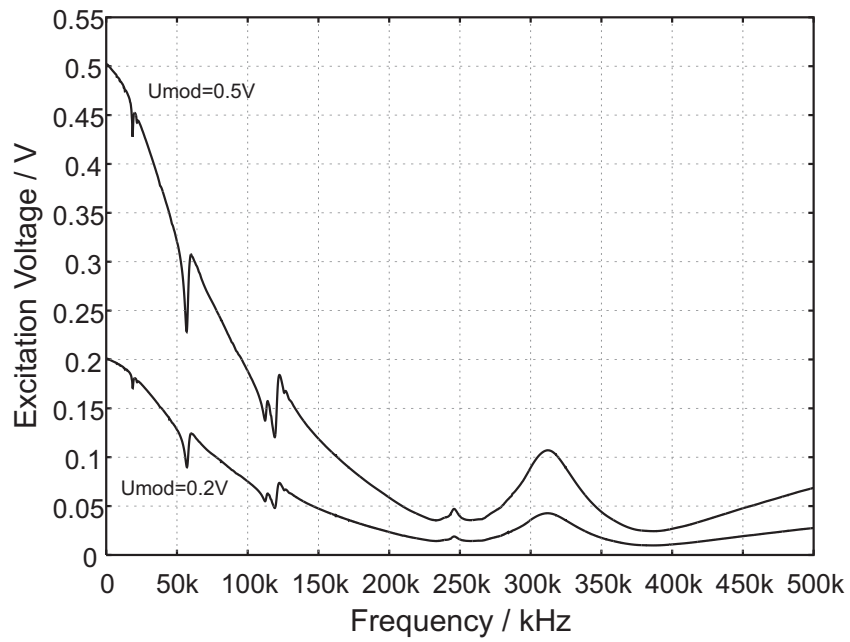


Figure 4.12: Electrical response on the modulation signal

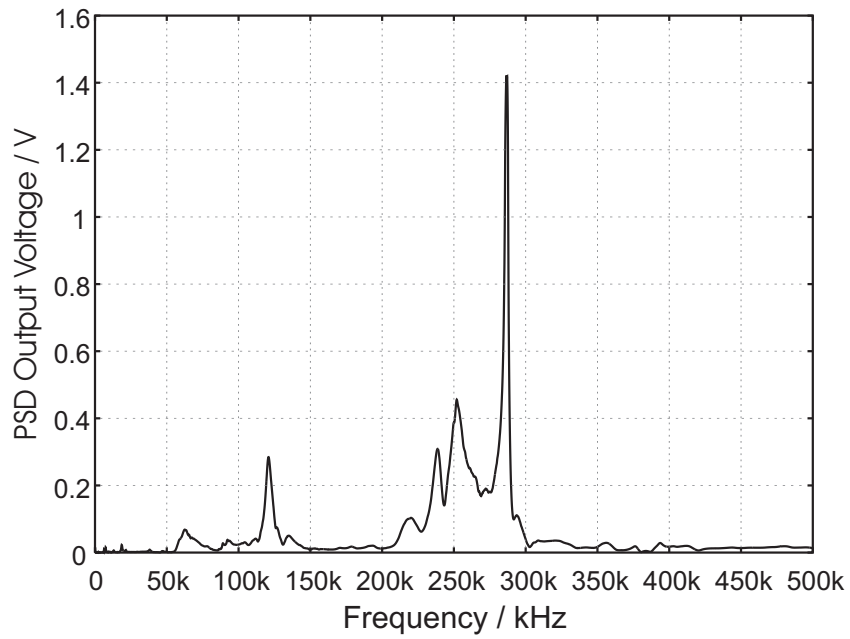


Figure 4.13: Mechanical response on the modulation signal

# 5 High resolution frequency analysis in Scanning Probe Microscopy

For the investigation of local material properties by the determination of the dynamic properties of a vibrating cantilever over a sample, a reliable frequency analysis system is required, which allows the determination of the complex transfer function (magnitude and phase) of the cantilever with sufficient resolution. Cantilever resonance frequencies range typically between 1 kHz – 500 kHz, with typical shifts of these resonance frequencies due to changes of the sample properties in the range of some Hertz.

Different frequency analysis systems can be used for the determination of the tip-sample interactions. Starting with the built-in instrumentation for dynamic mode imaging provided in most commercially available instruments, which are often implemented very simply<sup>1</sup>, fo-

---

<sup>1</sup>Some instrument designers had to introduce their own unit systems due to instrument design considerations

cussed on their main purpose the generation of an appropriate feedback signal for distance control, different existing external frequency analysis systems can be attached to the instrument, each of these systems with their own advantages and disadvantages. A brief overview of realization principles of frequency analysis systems is presented in this section to enable classification and comparison of the characteristic properties of the different realization principles under special consideration of SPM specific issues.

## 5.1 Frequency analysis systems for the characterization of dynamic properties

### 5.1.1 FFT-Spectrum-Analyzer

The use of fast fourier transformation (FFT) [61] is a common method for performing spectrum analysis. Most state-of-the-art digital storage oscilloscopes (DSO) are nowadays equipped by default with a frequency analysis option based on the FFT.

To perform a frequency analysis of a continuous input signal  $x(t)$ , the input signal is sampled with a sample frequency  $f_s$  producing a discrete dataset of  $N$  time domain samples  $x[n] = x(n \cdot T_s)$ , with  $n = 0, 1, \dots, (N - 1)$  and  $T_s$  as the sample time given by  $T_s = 1/f_s$ .

The discrete fourier transformation (DFT) is defined as

$$X(m, i) = \sum_{n=-\infty}^{\infty} x[n] \cdot g(i - n) \cdot e^{-j2\pi mn/N}, \quad (5.1)$$

where  $X(m, i)$  is a sample of the frequency dataset and dependent on

the frequency ( $m$ ) and the time ( $i$ ).  $g(i - n)$  is a weighting function, which is needed to fulfill the boundary conditions. Two boundary conditions for real FFT-analyzer must be taken into account for the acquisition of samples. One limitation is the power-on moment of the analyzer, samples older than this moment can't be acquired. The second limitation is given by the present time, as samples from the future also can't be acquired.

An appropriate window function, defined by  $g(i) = 1/N \cdot w(i)$ , must be provided. The window functions must be symmetrical, i.e.  $w(i) = w(N - 1) - i$ , and limited in such a manner that

$$w(i) = \begin{cases} 0 & \text{for } i \geq N \\ 0 & \text{for } i < 0 \end{cases} . \quad (5.2)$$

The rect-window defined by

$$w(i) = \sigma(i) - \sigma(i - N) , \quad (5.3)$$

with

$$\sigma(i) = \begin{cases} 1 & \text{for } i \geq 0 \\ 0 & \text{for } i < 0 \end{cases} \quad (5.4)$$

fulfills all these requirements and is the most common window function used in FFT-analyzers<sup>2</sup>. The DFT can then be written as

$$X(m, i) = \frac{1}{N} \sum_{n=i-(N-1)}^i x[n] \cdot e^{-j2\pi mn/N} \quad (5.5)$$

or as

$$X(m) = \frac{1}{N} \sum_{n=0}^{N-1} x[n] \cdot e^{-j2\pi mn/N} , \quad (5.6)$$

if the window shall not be floating [62], [63].

---

<sup>2</sup>Other window functions, like Blackmann-Harris and Hanning are also common and often used to reduce spectral leakage.

For practical considerations, the performance of FFT-analyzer can be determined by three key parameters, the number of input points  $N$ , the Nyquist frequency  $f_{NF}$  and the frequency resolution<sup>3</sup>  $\Delta f$ . These parameters are related as

$$f_{NF} = \Delta f \cdot \frac{N}{2} \quad (5.7)$$

and

$$\Delta f = \frac{1}{T_r} \quad (5.8)$$

where  $T_r$  is the sampling duration of the input waveform [64].

Estimating the efficiency of FFT-analyzer for the determination of the cantilever's frequency response, a frequency range of  $f_{NF} = 500kHz$  with a resolution of  $\Delta f = 1Hz$  has to be considered. The sample frequency of the FFT-analyzer must be chosen to be at least  $f_s = 1MHz$  in this case,  $N = 1E6$  data points have to be acquired in  $T_r = 1s$ . A relative modern digital sampling oscilloscope (DSO) with builtin FFT-analysis option is capable of the acquisition of up to 50.000 data points [64]. The acquisition time of 1s is very short, which is one main advantage of FFT-analyzers, but as for the complete frequency response of the cantilever this measurement has to be repeated at different driving frequencies, this advantage does not serve for this application. Most DSO provide only one channel for FFT-analysis making them rather useful for spectrum then for network analysis, though some instruments offers a phase spectrum measuring mode assuming a cosine carrier as excitation signal at the beginning of the acquisition process, which can be used for network analysis [64]. Dedicated FFT-analyzer are available on the market, providing two input channels,

---

<sup>3</sup>Also often referred as frequency increment.

which can be simultaneously sampled and FFT-transformed, enabling through calculation of the ratio of these channels the determination of the transfer function [65]. Concluding this discussion, FFT-analyzer are not feasible for the determination of tip-sample interactions under consideration of the above given parameters.

### 5.1.2 Lock-In Amplifiers

Lock-In Amplifiers (LIA) are widely used for the signal recovery of small repeating signals in the presence of larger interfering signals or noise. The system under test is excited for this purpose with a reference signal. The response is measured with a phase-sensitive-detector (PSD) with respect to this reference. The PSD is usually realized by a quadrature demodulation unit, as shown in Fig. 5.1. The reference signal is generated internally, but most LIA are also capable of synchronizing their reference signal by a phase-locked-loop (PLL) to an externally provided reference signal.

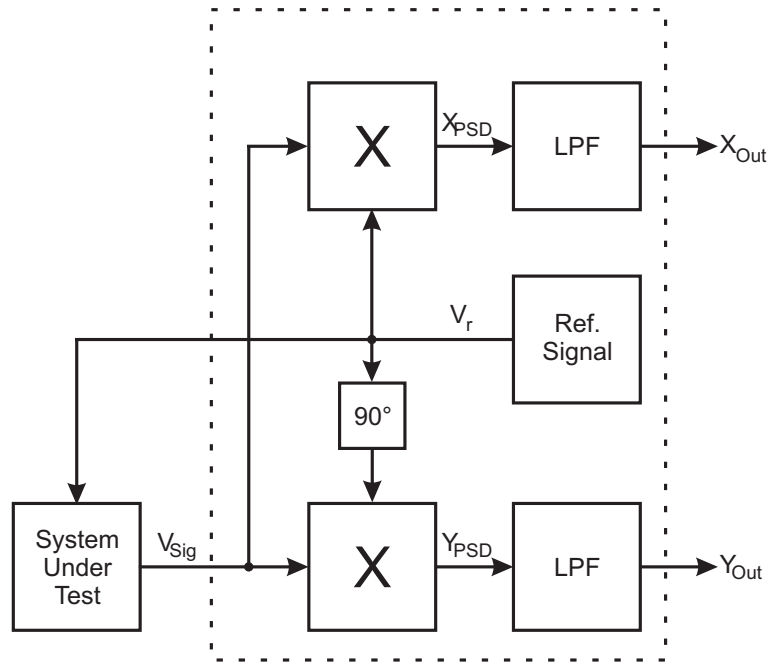


Figure 5.1: Principle Setup of a Lock-In Amplifier

According to the harmonic theorems [67] an input signal

$$V_{Sig} = V_0 \cdot \cos(\omega_{Sig}t + \varphi_{Sig}) \quad (5.9)$$

will be transformed to another frequency range, when it is multiplied with a reference signal

$$V_r = \cos(\omega_r t) . \quad (5.10)$$

The output signal of the upper phase-sensitive detector in Fig. 5.1 (X-Channel) will be

$$X_{PSD} = \frac{1}{2}V_0 (\cos([\omega_{Sig} - \omega_r]t + \varphi_{Sig}) + \cos([\omega_{Sig} + \omega_r]t + \varphi_{Sig})) \quad (5.11)$$

and after the removing of the upper sideband by low-pass filtering

$$X_{Out} = \frac{1}{2}V_0 \cos([\omega_{Sig} - \omega_r]t + \varphi_{Sig}) . \quad (5.12)$$

For the Y-Channel the reference signal is a sin function leading to

$$Y_{PSD} = \frac{1}{2}V_0 (\sin([\omega_{Sig} - \omega_r]t + \varphi_{Sig}) + \sin([\omega_{Sig} + \omega_r]t + \varphi_{Sig})) \quad (5.13)$$

and after low-pass filtering to

$$Y_{Out} = \frac{1}{2}V_0 \sin([\omega_{Sig} - \omega_r]t + \varphi_{Sig}) . \quad (5.14)$$

Calculating the magnitude

$$A = \sqrt{X_{Out}^2 + Y_{Out}^2} = \frac{1}{2}V_0 \quad (5.15)$$

and the phase

$$\varphi = \arctan\left(\frac{Y_{Out}}{X_{Out}}\right) = \varphi ; \text{ for } \omega_{Sig} = \omega_r \quad (5.16)$$

shows clearly, that the here presented quadrature detector allows the determination of magnitude and phase independent from each other, which is not possible if a LIA with a single PSD is used.

The effective measurement bandwidth of the LIA is dependent on the shape of the low-pass-filter (LPF). Bandwidths down to 0.01 Hz are possible [66], which reject noise signals and other undesired spectral components so that the signal of interest can be detected. For the determination of the cantilever's frequency response the reference frequency has to be swepted over the interesting frequency range.

### 5.1.3 Network Analyzer

Dedicated Network Analyzer, like the HP 4395A/4396B, are reference class instruments as well in performance as in price. They allow the examination of the frequency transmission properties with high resolution ( $\leq 1$  mHz,  $\leq 0.1$  dB) in a frequency range from 10 kHz up to

1.8 GHz [68]. Lower frequencies can be covered with an additional extension kit. The measuring bandwidth is dependent on the frequency range and can be as small as 1 Hz. The HP 4395A/4396B provides not a different method for frequency analysis, but rather a combination of an FFT analyzer and a sweeping demodulating analyzer. The analysis type is selected in accordance to the experimental parameter.

#### **5.1.4 Comparison of the different methods**

Simple FFT analyzer are not supposed to be sufficient for the desired application. Most systems do not provide the required resolution and lack also in the ability of measuring a complex transfer ratio.

Lock-In amplifiers are realized in different techniques and are available as low-cost analog devices, hybrid devices, which offer a digital interface for programming and data reception and state-of-the-art digital designs using modern digital signal processing techniques. Analog LIA require additional instrumentation for the conversion of the data into the digital domain, making the experimental setup more complicated. Common digital LIA have as major drawback a dependency of the frequency step size on the absolute frequency value, which especially in the kHz range does not provide sufficient frequency resolution. Furthermore, measurements made with these lockins are very slow, as the digital interface is not optimized for a fast transmission of data. Modern DSP-based lockin amplifiers do not own all these disadvantages, entering thus also a much higher price regime.

Network analyzer are also suitable for the present application, having as main drawback the high price of such a system, which is for

practical cases unacceptable high, as it is at least of the same order as a whole commercial SPM system.

Concluding this comparison, the design of a cheaper instrument, customized for the specific application with similar properties to the above discussed instrument types is highly desirable.

## **5.2 High resolution digital frequency analysis of dynamic properties in Scanning Probe Microscopy**

The realized system is presented in this chapter in detail, including an analysis of its properties. The system consists of a frequency analysis unit, a thermal control unit, and an additional system control unit, which provides the data interface to the controlling PC and allows the easy setup of the various parameters of the frequency analysis system. A simplified schematic setup of the frequency analysis system is shown in Fig. 5.2.

By the use of state-of-the-art digital signal processing components the system reaches an outstanding performance/price ratio, enabling the reliable determination of the dynamic properties of the tip-sample system in Scanning Probe Microscopy. The digital realization of the quadrature demodulation unit, avoids typical problems of other, mainly analog based, instruments used for dynamic analysis in SPM until yet.

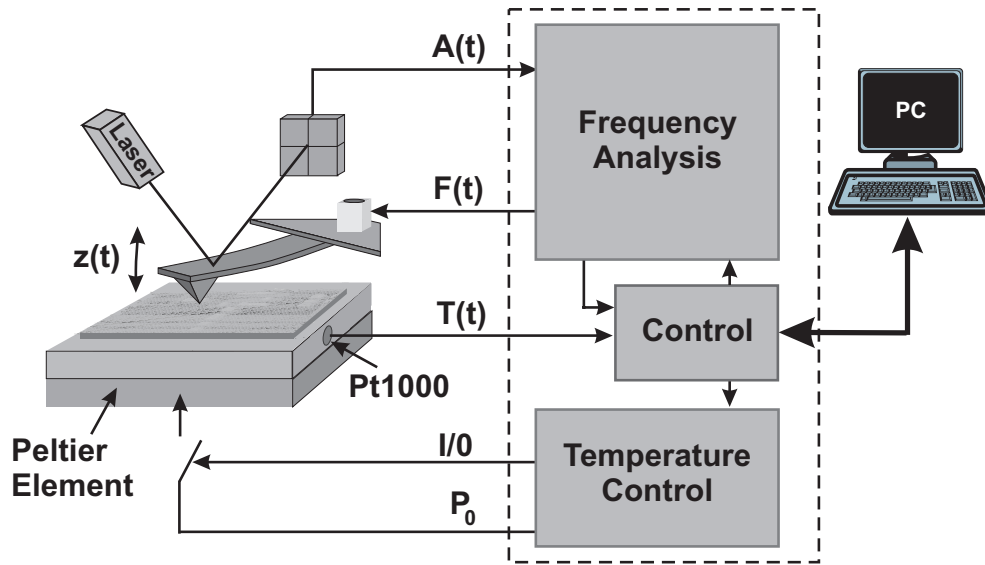


Figure 5.2: Schematic Frequency Analysis System Setup

The integration of the temperature control unit in this setup allows the examination of microscopic thermomechanical properties by studying the dynamic tip-sample behavior in relation to the temperature for a manifold variety of materials. For the desired investigation of polymers the local investigation of actually macroscopic defined characteristic parameters like the melting point  $T_M$  and the glass transition point  $T_G$  is feasible, which is very interesting especially for polymer blends consisting of different components.

## 5.2.1 Requirements on the electronics

### Frequency requirements

Cantilever resonance frequencies range, dependent on their force constant, between 10 kHz and 400 kHz defining thus the range to be

covered by the analysis system. The necessary frequency resolution is mainly determined by the Q value of the cantilever. In air, common cantilevers have a Q value of about 100, but in vacuum the quality factor can be up to 50,000. A worst case approximation of the latter case thus leads to a 3dB-bandwidth of 200 mHz. To be able to resolve at least 10 frequency points between the 3dB-bandwidth under this conditions, the frequency resolution should be better than 20 mHz. This will allow a safe determination of the resonance frequency.

### **Thermal requirements**

The definition of the system requirements for the thermal control unit are not so straightforward, as they are highly dependent from the sample's properties which are to be investigated. For the desired investigation of polymers e.g., it must be considered that polymers are often specially designed to have a particular thermal behavior. Characteristic points, like the glass transition point or the melting point, can thus vary over a wide temperature range, from temperatures below room temperature up to 1000° C. The temperature range between -50° C and 150° C and the temperature resolution of 1° C are thus chosen more or less arbitrarily as a compromise between covering a wide application area, and limiting the requirements on the instrumentation side to common available components.

### **Interface requirements**

Another important issue for the instrument designer is the interface between the frequency analysis system and the microscope. Almost

every commercial SPM manufacturer provides a more or less open external modulation input. In the used *Topometrix Explorer System* this is coupled to the piezo as shown in section 4.4. For the modulation output of the frequency analysis system this means, that the output must be capable of driving the capacitive load in respect of stability and current. The detector signal of the position sensitive detector is amplified by the first stage amplifier, as shown in section 4.3, and fed after this to a difference amplifier, which forms the difference signal between the two upper and the both lower PSD elements (T-B signal) and also the difference signal between the two left and the two right PSD elements (L-R signal). The T-B signal is available at the output of the first stage of the ECU and is fed from there to the frequency analysis system.

## **5.2.2 Realization of the digital frequency analysis system**

### **Frequency analysis unit**

The frequency analysis unit is divided in two parts. A *preamplifier* stage contains the analog input channel with all necessary components for the processing of the analogue signal, including the ADC. The preamp stage is connected as an add on card to the *analyzer* stage, providing so the easy possibility to customize the system for other purposes simply by changing the preamp stage. An overview of the complete frequency analysis unit is shown in Fig. 5.3.

The signal is AC-coupled into the preamp stage to remove the DC-

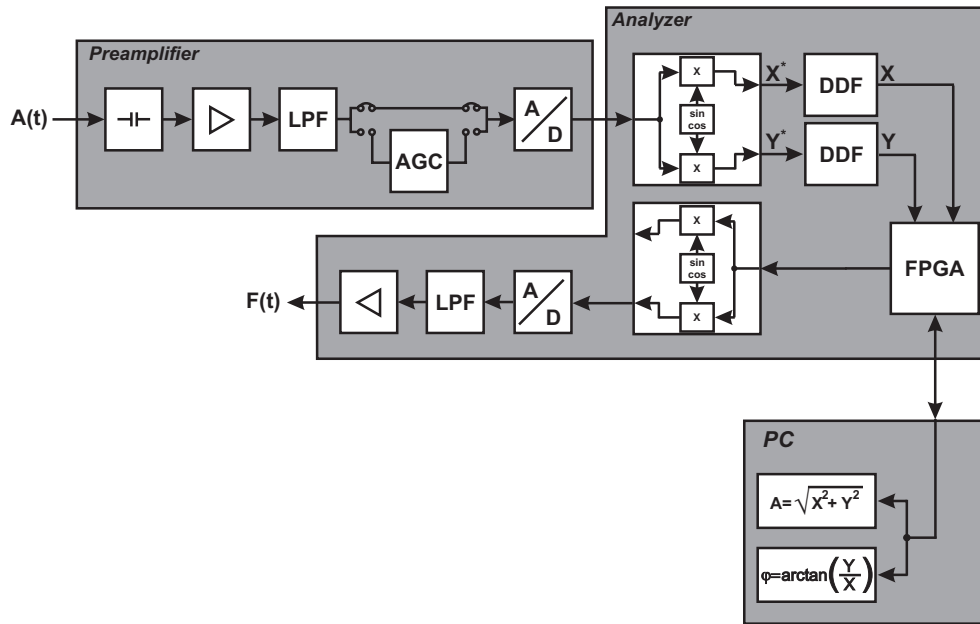


Figure 5.3: Frequency Analysis Unit

offset, which exists if the laser is not aligned ideally to the center of the PSD. An adjustable amplifier allows the calibration of the input and is followed by an anti-aliasing low-pass filter. The signal can be routed through an optional automatic gain control stage (AGC), to allow, if necessary, a software controlled attenuation before it is digitized by the ADC. The output of the ADC is routed via buffer registers to the analyzer stage. The design, so far described here, is straightforward.

The input stage is shown in Fig. 5.4. The AC-coupling is realized by a simple RC-element, formed by  $C_{24}, C_{74}, C_{75}$  and  $R_{12}, R_{69} - R_{72}$ . It is followed by the operation amplifier  $OP_1$ , which works mainly as impedance converter with adjustable amplification. The input filter is realized by a passive elliptic low-pass of 5th order with 6 dB passband attenuation. The passband attenuation is compensated by ap-

appropriate adjustment of the amplifier  $OP_1$ . The cut-off frequency of

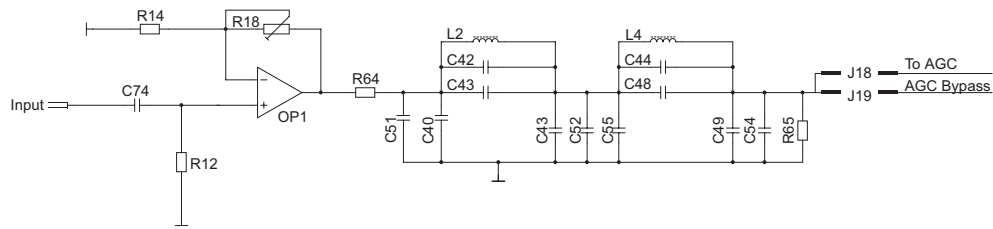


Figure 5.4: Preamplifier Input Stage

the low-pass is chosen to be 10 MHz, which allows the transmission of the desired frequency range (0–1MHz) with negligible phase shift. Special care has been taken to suppress the system clock frequency. The optional AGC block is realized with an analog multiplier. The

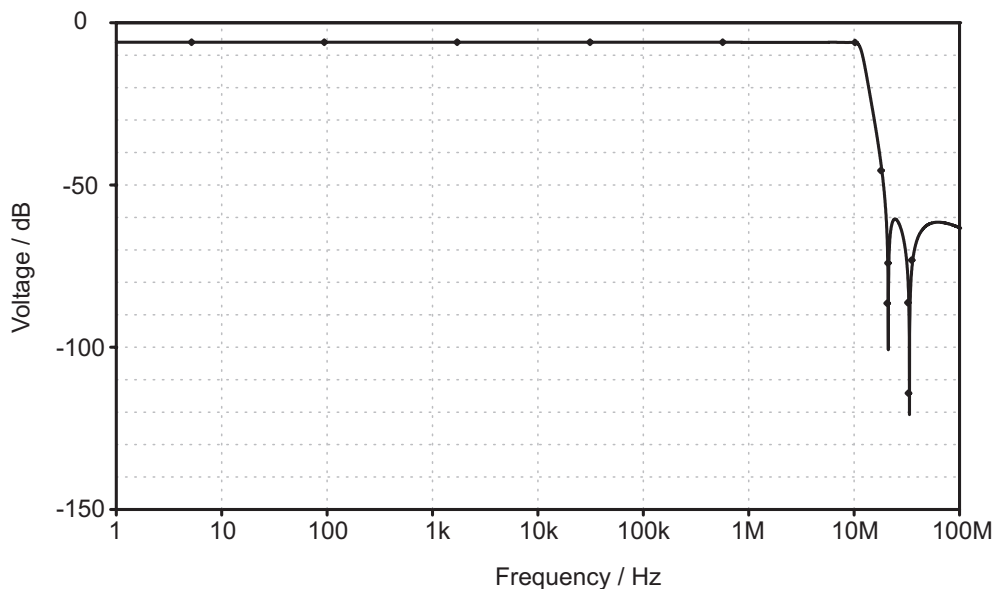


Figure 5.5: Simulated frequency response of the preamp input filter

input signal is fed to the first multiplier input, the output voltage of a 10 bit digital-to-analog converter (DAC) is connected to the second multiplier input. By controlling the DAC output voltage via PC a user

programmable signal attenuation is provided. As the preamp board was specially designed to fit the output voltage level of the SPM photodetector, the AGC block was not used and the preamp was jumpered in AGC bypass mode, but the AGC may be useful in other experiments. The last processing stage of the preamp board is the ADC, which converts the input signal to the digital domain. It provides 14 bit resolution at an input voltage level of  $V_{pp} = 2.2V$  and a typical signal-to-noise-ratio (SNR) of 74 dB at a bandwidth of 10 MHz. The decrease of the bandwidth in the following processing stages improve this SNR significantly.

The digital input signal is fed to the numerically controlled oscillator / modulator (NCOM) for demodulation. The NCOM consists basically of a sin/cos generator and a quadrature demodulator stage. Unlike other devices, the chosen NCOM is working completely in the digital domain and allows the digital demodulation of the receiving signal immediately down to the baseband. Similar other devices have usually an integrated DAC in the output stage of the modulator, making them more or less useless for digital demodulation. Analog demodulators, especially analog quadrature demodulators, often lack in terms of crosstalk and linearity.

One delicate component of analog demodulators is the generation of the in-phase and quadrature carrier, when an ideal  $90^\circ$  phase shift shall be maintained over a wide frequency range, as needed for spectrum analysis purposes. Due to the digital generation of the inphase and quadrature carrier, based on the *Direct Digital Synthesis* (DDS) method with 32 bit frequency resolution, this process is trivial for the realized system. Another main challenge for analog demodulators is

the realization of the mixer. Semiconductor mixer leak often in terms of offset and thermal drift making it a big challenge for the designer to achieve good system performance. Mixing in the NCOM is a numerical operation performed with fixed point numbers. The achieved performance is limited by the numerical word length, which is 16 bit for the input words and 33 bit for the output words.

A significant performance improvement is achieved in the present design, by transferring the demodulation process completely into the digital domain. The overall achieved SNR for the NCOM is given with better than 90 dBc [76]. Beside the excellent performance in AM-demodulation, the presented design allows the easy implementation of further modulation techniques. Fig. 5.6 shows the structure of the device with its main components: the phase and frequency control section (PFCS), the phase accumulator, the sin/cos generator, and the complex multiplier and accumulator (CMAC).

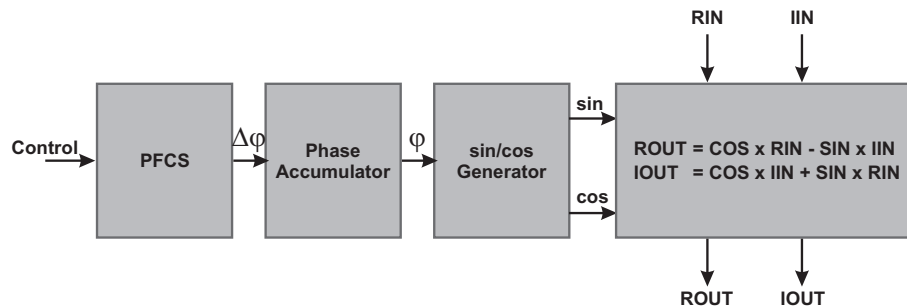


Figure 5.6: NCOM Overview

The PFCS is shown in detail in Fig. 5.7. Three 16 bit input registers can be loaded by a 16 bit control bus. The outputs of two of them are joined together to form a 32 bit frequency word which can be loaded

either to the *Center Frequency Register* or to the *Offset Frequency Register*. The third input register, the *Phase Input Register*, can be used for continuous phase modulation. Alternately, by switching a multiplexer activating the *Quad Phase Shift Keying Encoder (QPSK)*, fixed phase shifts in 90 degree steps can be applied by control of two bits.

The phase register and the QPSK encoder are used in the present application to adjust the phase between the reference signal and the input signal. On the frequency register side another multiplexer controls, whether the offset frequency register shall be added to the center frequency or not. By controlling this offset frequency multiplexer, frequency shift keying (FSK) modulation can be performed. The use of this function in SPM experiments allows the acquisition of the fundamental cantilever spectrum and the spectrum of higher harmonics more or less simultaneously by changing the receiver frequency between two frequency steps of the excitation frequency.

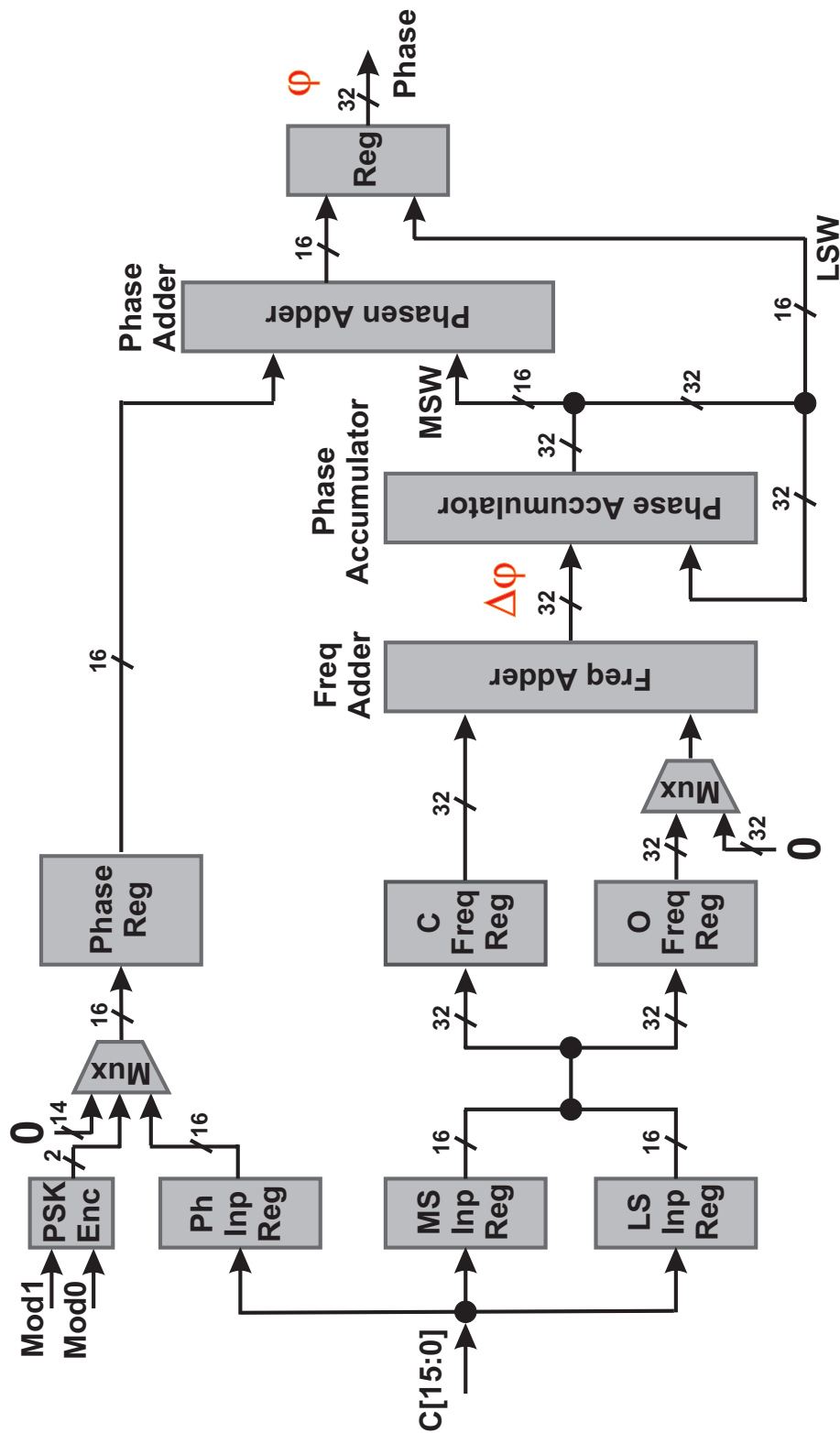


Figure 5.7: NCOM phase and frequency control section (PFCS)

The sum of the center and offset frequency is the so-called phase increment  $\Delta\varphi$ . It is fed to the phase accumulator which calculates according to this phase increment the appropriate phase value in dependence on time for the chosen frequency. With the phase address following the phase accumulator, a phase modulation either continuous or as QPSK can be performed. The effective phase value is fed to the sin/cos generator section which provides the appropriate amplitude value of the in-phase and quadrature reference signal for the demodulator.

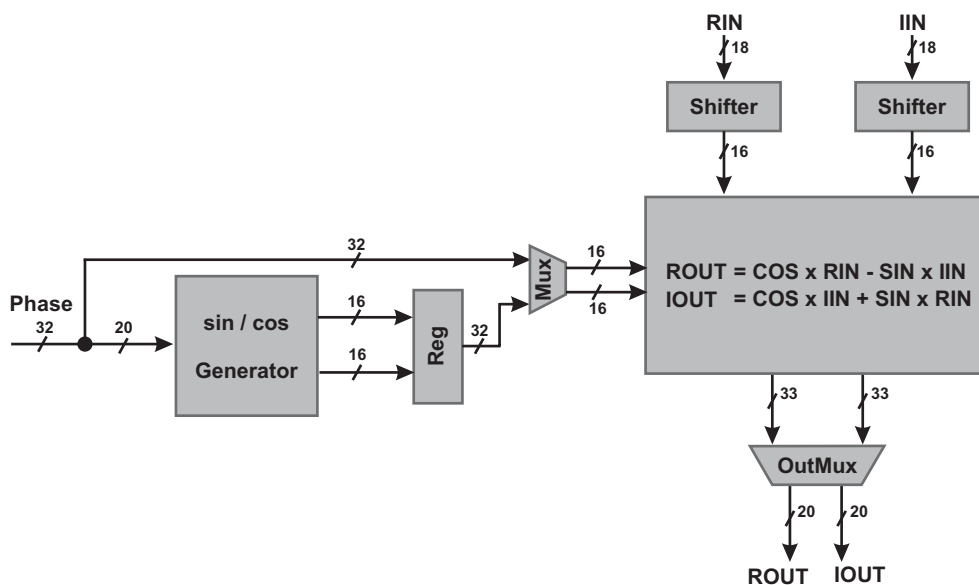


Figure 5.8: NCOM SIN/COS Generator and CMAC

The input signal is routed via a barrel shifter to the CMAC, which performs the complex operations

$$R_{Out} = R_{IN}(\omega, t) \cdot \cos(\omega_r t) - I_{IN}(\omega, t) \cdot \sin(\omega_r t) \quad (5.17)$$

$$I_{Out} = I_{IN}(\omega, t) \cdot \cos(\omega_r t) + R_{IN}(\omega, t) \cdot \sin(\omega_r t) . \quad (5.18)$$

These equations are simplified in this case to

$$R_{Out} = R_{IN}(\omega, t) \cdot \cos(\omega_r t) \quad (5.19)$$

$$I_{Out} = R_{IN}(\omega, t) \cdot \sin(\omega_r t) \quad (5.20)$$

as the imaginary input is not used in this application and set to zero, leading, if  $\omega_r = \omega$  is chosen, to the in-phase and the quadrature component of the demodulated signal. For other combinations, e.g.  $\omega_r = 2\omega$ ,  $\omega_r = 3\omega$ , higher harmonics of the input signal will be obtained.

At the output of the NCOM, which consists of two channels with 20 bit word length each, the demodulated data are present with a data rate of 20 MSamples per second. As shown in Section 5.1.2, this data stream has to be filtered by a low-pass filter to eliminate the upper sideband. Furthermore the data rate has to be reduced to a value transferable and processable by a PC. Both operations are performed by two *Digital Decimation Filters* (DDF) which are connected to each output of the CMAC. Fig. 5.9 shows a coarse overview of the DDF structure.

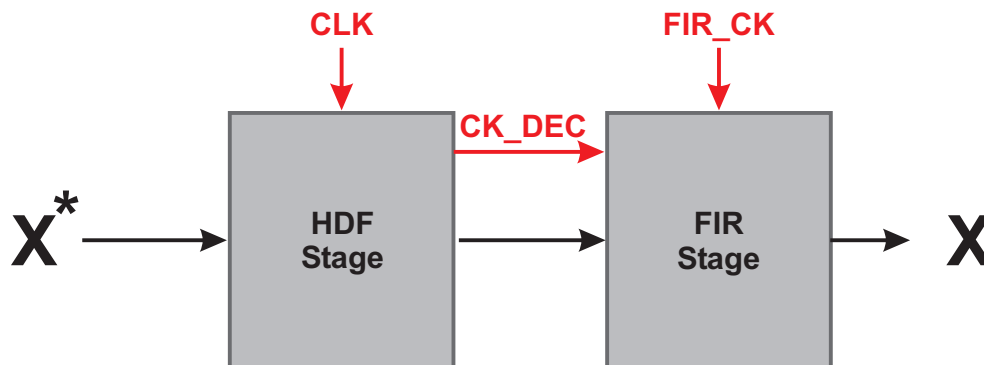


Figure 5.9: Structure of the Digital Decimation Filter

The DDF consist of two blocks, a *High Order Decimation* (HDF) block, which performs a coarse low pass filtering and the main part of decimation, and a *FIR filter* block which provides the final shaping of the low-pass transfer function and some additional decimation.

The HDF section is capable of performing a decimation factor of up to 4096. In combination with the FIR stage the maximum decimation ratio can reach 16384. The FIR stage is completely user programmable and can have an order up to 512. The configuration of the filter is variable over a wide range but limited by several parameters, like the above mentioned values. By use of a filter design software, transfer functions can be designed under consideration of application dependent parameters rather than device specific parameters. The following table and Fig. 5.10 show several designed transfer functions used to perform the measurements in this work.

Filter Parameter	a	b	c
Passband	30 Hz	300 Hz	1 kHz
Transition Band	175 Hz	250 Hz	900 Hz
Passband Attenuation	0.01 dB	0.01 dB	0.01 dB
Stopband Attenuation	80 dB	100 dB	100 dB
Input Sample Rate	20 MHz	20 MHz	20 MHz
FIR Input Rate	20 kHz	20 kHz	80 kHz
Output Rate	2 kHz	5 kHz	10 kHz

Table 5.1: Filter parameter for typical DDF transfer functions

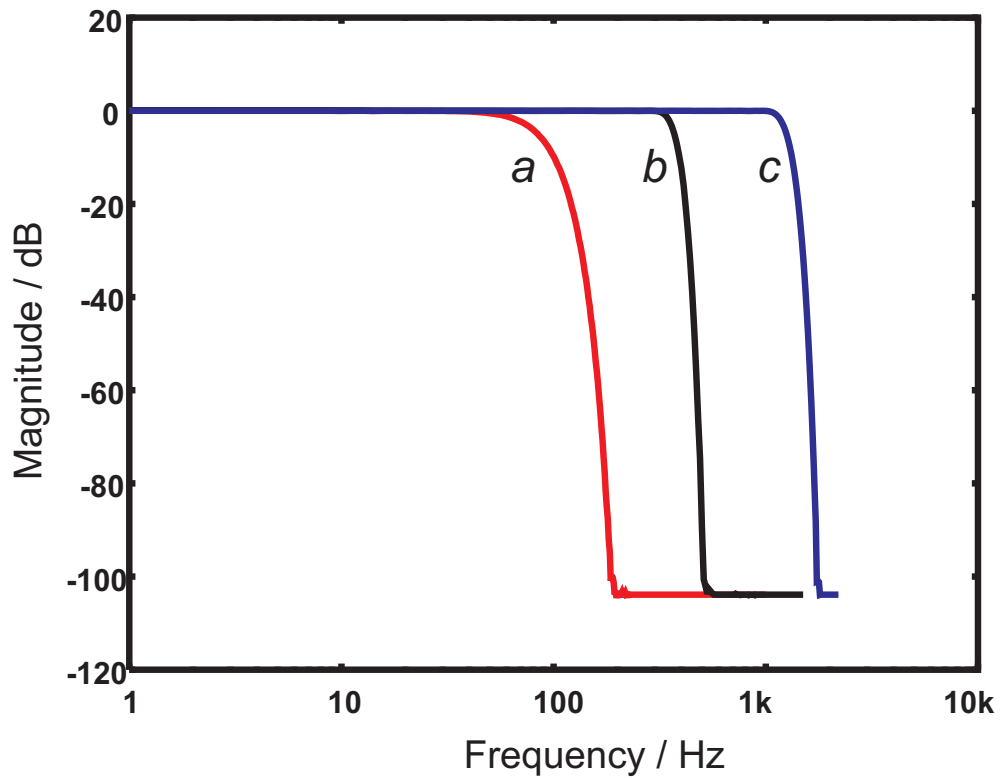


Figure 5.10: Different transfer functions realized with the DDF

The output data of the DDF filter have a word length of 24 bit per channel and, according to the above presented parameter, at a data rate between 2 – 10 kHz.

The DDF output data are sampled by the *Field Programming Gate Array* (FPGA), customized as system controller, and transferred to the PC using the standardized *Enhanced Parallel Port* interface, according to the IEEE 1284 specification. Inside the PC the received real and imaginary parts of the system response are transformed to a magnitude / phase pair, visualized and stored for further processing.

For the digital generation of the reference signal a second NCOM is

used. The modulation abilities of the NCOM are not necessary for this purpose, and so the modulation inputs are used to adjust the oscillation amplitude. The output of the NCOM is converted to the analog domain via a 16 bit DAC and filtered by a reconstruction low-pass, as already used for the preamp input stage. A line driver, as shown in Fig. 5.11, drives the capacitive load of the piezo. The FPGA controlled *Piezo Offset Line* in Fig. 5.11, allows the application of an additional digital 5V offset voltage at the piezo element and thus enables the adjustment of a determined tip-sample distance for the experiments.

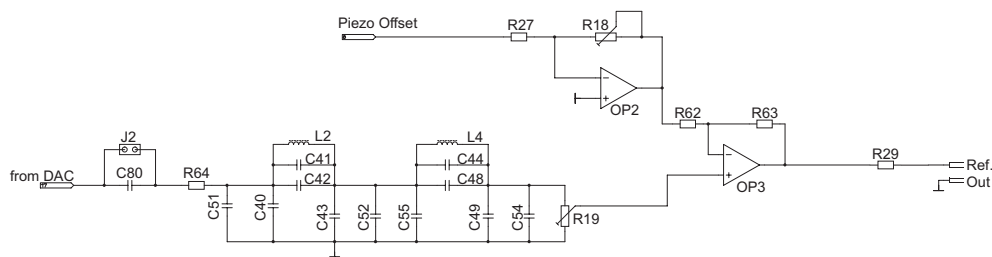


Figure 5.11: Reference Output Instrumentation

Calibration of the frequency analysis system was performed first using a HP 33120A Function / Arbitrary Waveform Generator for the calibration of the receiver, a Tektronix TDS 300 Digital Sampling Oscilloscope and a HP 4395 B Network Analyzer for the calibration and analysis of the reference output. Next, the realized analyzer was used to analyze its own transfer function, which is shown in Fig. 5.12 and 5.13.

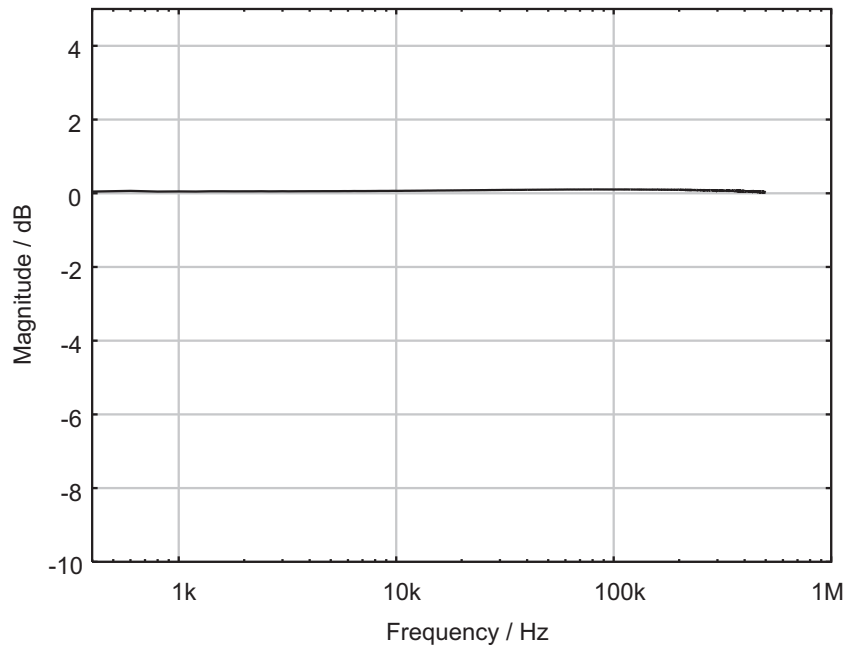


Figure 5.12: Magnitude Calibration Spectrum

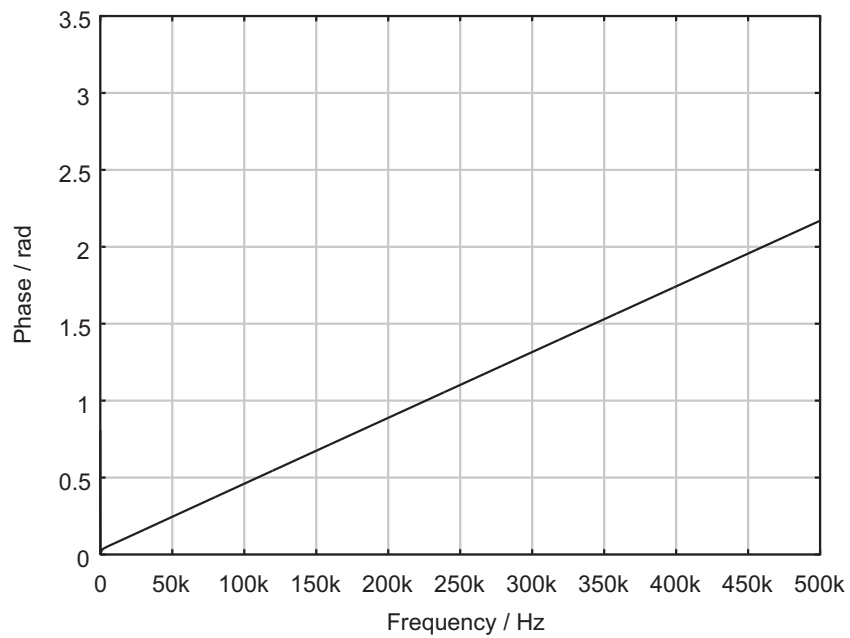


Figure 5.13: Phase Calibration Spectrum

The magnitude spectrum is plotted on a logarithmic scale, while a linear scaling for the phase spectrum is selected to show the linear dependency of the phase shift over the frequency. The linear dependency is associated with a constant group delay, caused by the several pipeline stages in the system.

### Frequency resolution

For the examination of the frequency resolution of the realized system, measurements on quartz tuning forks have been performed. Tuning forks are becoming of increasing importance in Scanning Probe Microscopy. They are widely used for distance control in Scanning Nearfield Optical Microscopy (SNOM) [77], [78] and recently also as probes in force microscopy for very high resolution imaging [79], [60].

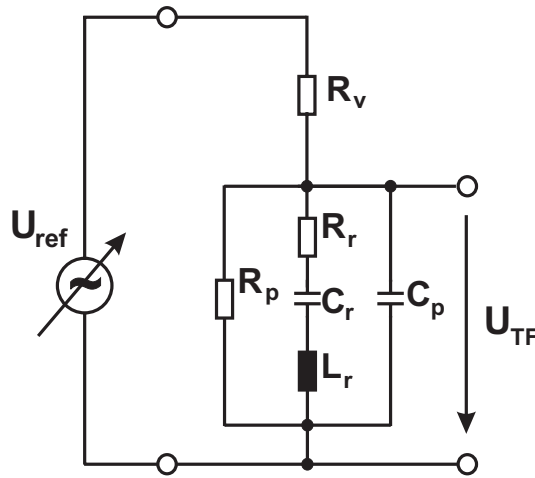


Figure 5.14: Setup for the investigation of tuning forks

Due to their high quality factor, the frequency behavior of unprepared tuning forks cannot be measured with usual frequency analysis tools used in Scanning Probe Microscopy. Using the setup shown in Fig.

5.14 the response of a tuning fork, forming a voltage divider with resistor  $R_v$ , was measured.

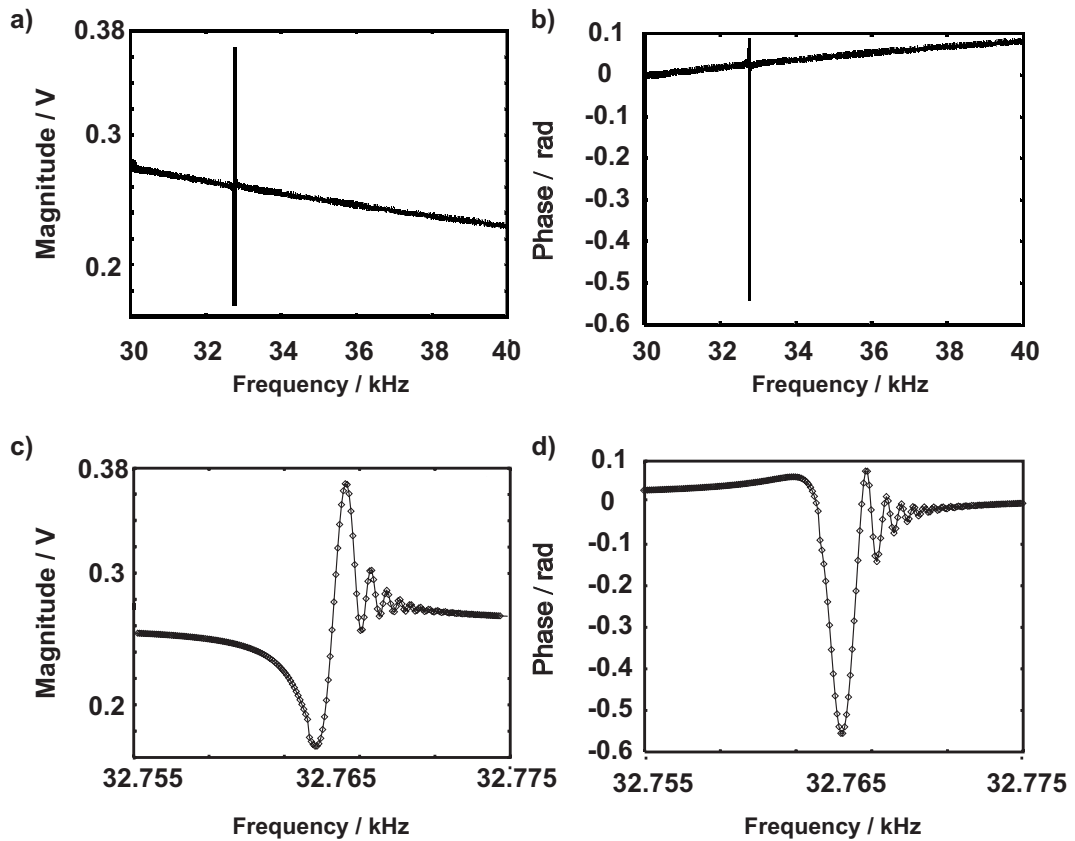


Figure 5.15: Magnitude and phase spectrum of a tuning fork (measured at  $U_{ref} = 0.5V$ )

The magnitude spectrum is shown Fig. 5.15 a) and phase in Fig. 5.15 b). As these measurements were performed with a frequency resolution of 0.1 Hz, Fig. 5.15 c) shows a zoom of the spectrum a) and d) respectively a zoom of b). Both resonance frequencies of the tuning fork, the serial resonance at the minimum voltage and the parallel resonance where the voltage at the tuning fork reaches a maximum. The ringing after the both maxima is caused by the high sweep rate,

which was used to perform this measurement. The maximum achievable frequency resolution of the realized system is given by

$$f_{step,min} = \frac{f_{CLK}}{2^{32}} = \frac{20MHz}{2^{32}} \approx 4mHz . \quad (5.21)$$

### Noise considerations

The signal-to-noise-ratio (SNR) is estimated using Fig. 5.16 and by assuming white noise distribution.

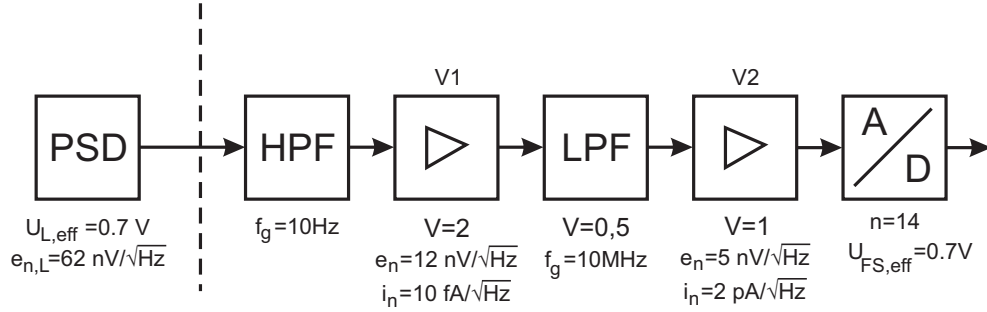


Figure 5.16: Noise Considerations of the analog part

The contribution of the first amplifier of the preamp stage (V1) is given with  $e_{n,V1} = 12nV/\sqrt{Hz}$  for the voltage noise density and a current noise density of  $i_{n,V1} = 10fA/\sqrt{Hz}$ , working worst case on a resistor of  $R_{HPF} = 1M\Omega$  and thus leading to an equivalent voltage noise density of  $e_{n,i,V1} = 10nV/\sqrt{Hz}$ . The differential ADC driver (V2) is given with a voltage noise density of  $e_{n,V2} = 5nV/\sqrt{Hz}$  and a current noise density of  $i_{n,V2} = 2pA/\sqrt{Hz}$ , working on a resistor of  $R_{Diff} = 250\Omega$  and thus leading to an equivalent voltage noise density of  $e_{n,i,V2} = 0.5nV/\sqrt{Hz}$ . The effective noise density of the ADC is given approximately as

$$e_{n,ADC} = \frac{U_{FS}}{2^n \cdot \sqrt{12}\sqrt{B}} = \frac{0.7V}{2^{14} \cdot \sqrt{12} \cdot \sqrt{10MHz}} \approx 4nV/\sqrt{Hz} . \quad (5.22)$$

The effective noise density of the complete analog part of the realized system is thus approximately given as

$$e_{n,A} = \sqrt{e_{n,V1}^2 + e_{n,i,V1}^2 + e_{n,V2}^2 + e_{n,i,V2}^2 + e_{n,ADC}^2} \approx 16nV/\sqrt{Hz}. \quad (5.23)$$

Assuming additionally a typical light current of  $I_L = 50\mu A$ , as referred in section 4.3, leading after the PSD first stage amplifier to a voltage of  $U_{L,eff} = 0.7V$ , the associated shot noise current<sup>4</sup> will be transferred to an effective noise density of  $e_{n,L} = 62nV/\sqrt{Hz}$ .

The effective noise density under consideration of the photodetector is thus estimated to be

$$e_{n,(A+PSD)} = \sqrt{e_{n,L}^2 + e_{n,A}^2} = 64nV/\sqrt{Hz} \quad (5.24)$$

As clearly visible, the effective noise density is dominated by the noise properties of the photo sensitive detector. The noise of the instrument is negligible. The so far calculated noise density is working over a bandwidth of 10 MHz, determined by the cutoff frequency of the anti-aliasing filter, and generates at the input of the ADC a noise voltage of

$$U_{n,(A+PSD)} = e_{n,(A+PSD)} \cdot \sqrt{B} = 203\mu V, \quad (5.25)$$

which is equivalent to two bits of noise. The signal-to-noise ratio at this point is

$$SNR_{(A+PSD)} = \frac{U_{Sig}}{U_{n,(A+PSD)}} = \frac{0.7V}{203\mu V} \approx 3448 \hat{=} 71dB. \quad (5.26)$$

The contribution of the digital part of the analyzer is negligible, especially according to the noise properties of the photo sensitive detector.

---

<sup>4</sup>Which is here assumed to be the dominant contribution of the PSD noise

As the used word length is at least 16 bit, the occurrence of rounding effects, which could contribute also to the effective noise density, is avoided. The most important influence of the digital part is thus the bandwidth reduction. Assuming that the DDF filter works as an ideal low-pass filter<sup>5</sup>, the effective bandwidth is determined by these filters. The noise voltage after the DDF stage, programmed to have a bandwidth of 30 Hz, is thus  $U_{n,DDF} = 350nV$ . The signal to noise ratio after DDF filtering is given to

$$SNR_{DDF} = \frac{U_{Sig}}{U_{n,DDF}} = \frac{0.7V}{350nV} \approx 2 \cdot 10^6 \hat{=} 126dB, \quad (5.27)$$

assuming that the full scale input of the ADC is used. If the noise contribution of the photo-detector is not considered and thus the analyzer specific SNR is calculated, a SNR of 138 dB is obtainable.

The resolution of the magnitude and phase can be calculated as

$$\Delta A_n = \pm \sqrt{X^2 + Y^2} = \sqrt{2U_{n,DDF}^2} = \pm 495nV, \quad (5.28)$$

corresponding to an SNR of 123 dB, and

$$\Delta \varphi_n^* = \pm \arctan\left(\frac{Y}{X}\right) = \arctan\left(\frac{U_{Sig} - U_{n,DDF}}{U_{Sig} + U_{n,DDF}}\right) \quad (5.29)$$

$$= \pm \arctan(0.999999) = \pm 44.99997135^\circ \quad (5.30)$$

$$\Delta \varphi_n = 45^\circ - (\pm 44.99997135^\circ) = \pm (28 \cdot 10^{-6})^\circ \quad (5.31)$$

### Thermal analysis unit

The thermal analysis unit allows measurement and control of desired temperature profiles. It consists of a temperature measurement block,

---

<sup>5</sup>Which is a good assumption in respect to their performance

a temperature control block and a temperature model block. The model block defines the temperature profile in dependence on time, the PID controller block compares the model temperature with the actual measured temperature and outputs a pulse width value for the PWM controlled heat/cooling source to adjust the measured temperature to the model temperature. As the model block is realized completely in software, arbitrary temperature profiles are applicable to the sample. Fig. 5.17 shows a overview of the temperature analysis unit.

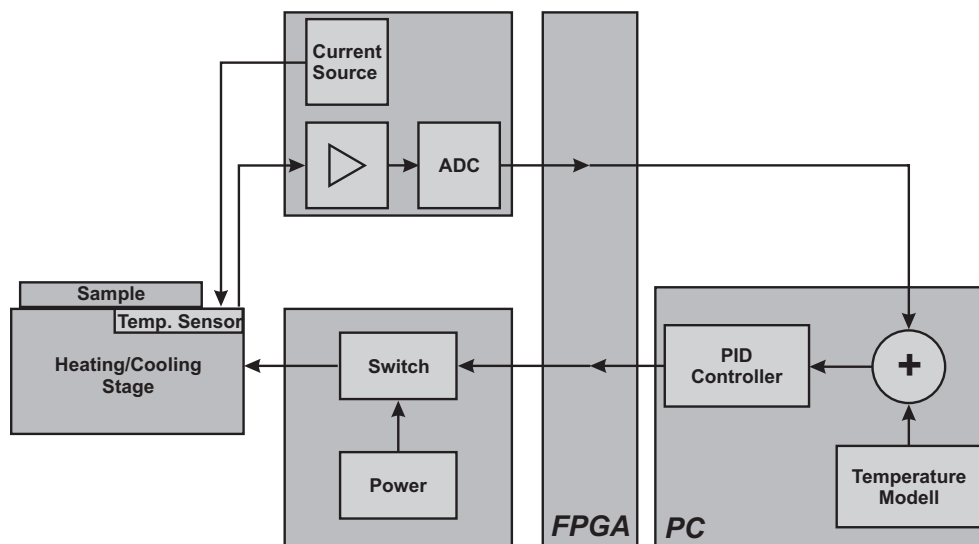


Figure 5.17: Overview of the temperature analysis unit

A PT1000 resistor thermometer, according to DIN EN 60751, class 1/3 B, is used as temperature element, as these sensors are more sensitive than the usually used PT100 elements. As the PT1000 element is fixed inside the copper sample carrier, some millimeters below the sample, it does not measure the real sample temperature but the difference is expected to be negligible. To avoid errors due to the cables

resistances between sensor and measurement block, a stable current source is used to apply a constant current of about  $123.5\mu A$  on the sensor, the sensor voltage is measured by an amplifier with high input impedance. The relative small current flowing through the sensor prevents the sensor element from self-heating and minimizes errors caused by the resistance changes due to the operation.

### Temperature measurement

Fig. 5.18 shows the realization of the measurement block. The current source is formed by the voltage reference *IC9*, transistor *T2*, the operation amplifier *IC7-1* and *R6*. The current is given by

$$I_{const} = \frac{U_{ref}}{R_6}, \quad (5.32)$$

where  $U_{ref}$  is the reference voltage provided by *IC9*. The current flows through the multiplexer *IC11* and can thus be routed to one of up to 6 different sensor elements. Position No. 7 and 8 of the multiplexer are connected with the reference resistors *R7* and *R8*, which are used to calibrate the measurement chain. The values of *R7* and *R8* are selected to represent the appropriate resistances of PT1000 elements for  $-40^\circ C$  and  $150^\circ C$ . The voltage of the chosen sensor is routed via *IC10* to the opamp *IC7-4*, where an offset correction is performed. The offset correction factor can be adjusted by *R55*. The corrected voltage is fed, after low-pass filtering with the RC combination *R35*, *C94*, to a 10 bit ADC where it is converted to the digital domain.

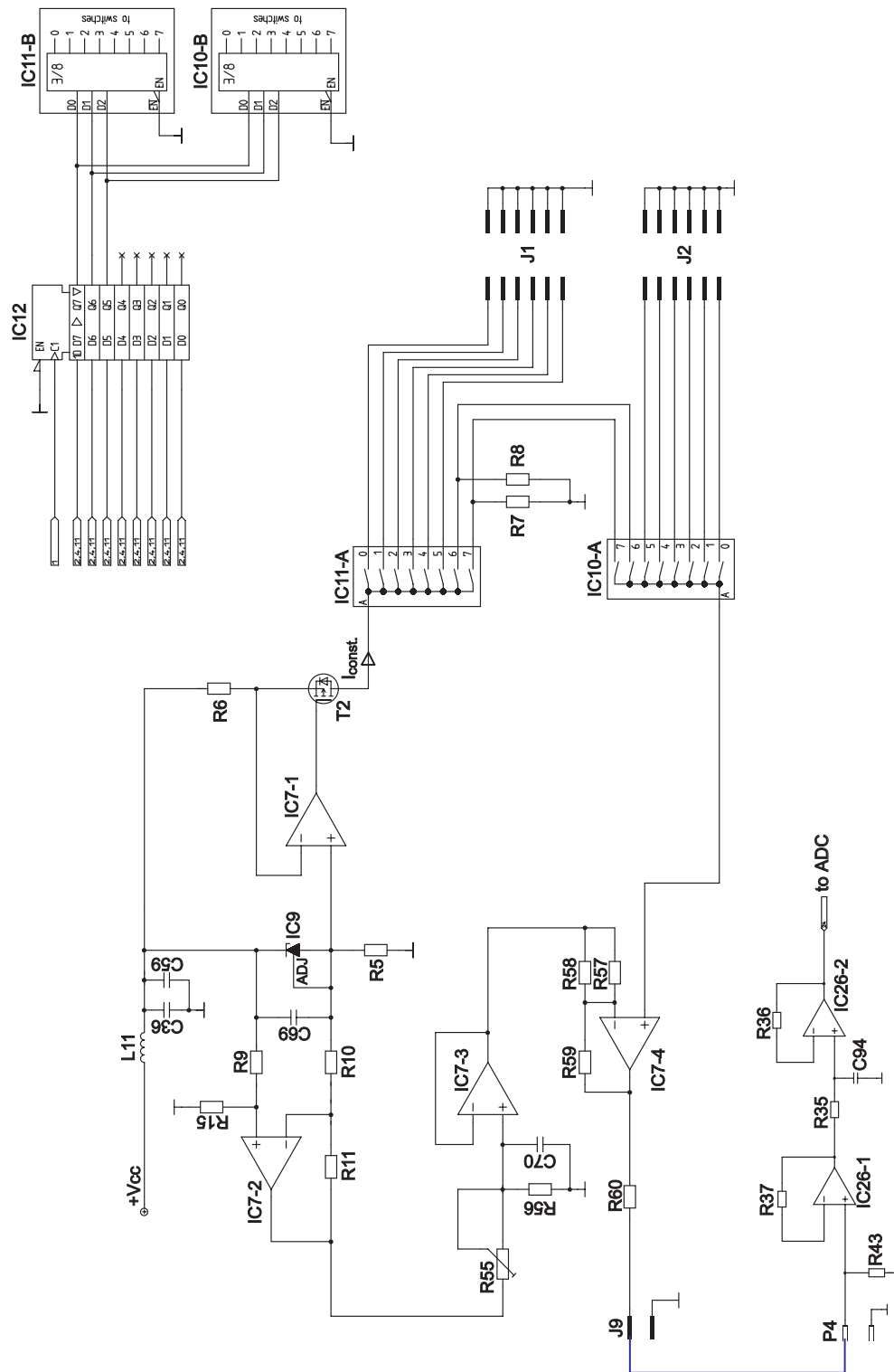


Figure 5.18: Realization of the temperature measurement block

The dependence between the temperature and the resistance can be expressed by a Taylor series<sup>6</sup> to

$$R_{PT} = R_0 \cdot (1 + \alpha \cdot \Delta T) , \quad (5.33)$$

where  $\alpha$  is the temperature coefficient of platin<sup>7</sup>. The temperature can thus be calculated from the resistance as

$$T = \frac{1}{\alpha} \left( \frac{R_{PT}}{R_0} - 1 \right) . \quad (5.34)$$

The transfer function of the temperature measurement block is given by

$$U_{Temp} = R_{PT} \cdot I_{const} \cdot V_p - U_n \cdot V_n , \quad (5.35)$$

where  $V_p$  is the amplification factor of the positive branch and  $V_n$  the amplification factor of the negative branch of *IC7-4*.  $U_n$  is the offset voltage formed by *IC9*, *IC7-2* and *R55*, *R56*.

As  $U_n$  and  $I_{const}$  can vary, dependent on device tolerances and environmental parameters, from the calculated theoretical values, *R7* and *R8* are used to calibrate the thermometer. For calibration, the equation

$$\begin{pmatrix} U_{a1} \\ U_{a2} \end{pmatrix} = \begin{pmatrix} R_7 \cdot V_p & -V_n \\ R_8 \cdot V_p & -V_n \end{pmatrix} \begin{pmatrix} I_{const} \\ U_n \end{pmatrix} \quad (5.36)$$

is solved.

With the well-known values of the resistors and the transfer functions for the positive and negative branch, the constant current and the offset voltage can be calculated  $I_{const}$  as

$$I_{const} = \frac{U_{a1} - U_{a2}}{V_p(R_7 - R_8)} \quad (5.37)$$

---

<sup>6</sup>Which is truncated here after the first term

<sup>7</sup> $\alpha = 0,003851/K$

and for  $U_n$  as

$$U_n = \frac{U_{a1} \cdot R8 - U_{a2} \cdot R7}{V_n(R7 - R8)} . \quad (5.38)$$

### **Temperature model**

The temperature profiles used for the analysis of thermal sample properties are based on a simple temperature model which is realized completely in software. For the present measurements only linear profiles were used as defined by the function

$$T_{Set}(t) = G \cdot t + T_0 , \quad (5.39)$$

but as this function is defined in the control software arbitrary profiles are possible.  $G$  is the used defined temperature gradient, which was for the performed measurements between 0.5 K/min and 4 K/min,  $t$  is the time and  $T_0$  the start temperature.  $T_0$  is simply defined by measuring the actual temperature at the begin of a temperature profile acquisition.

### **Temperature control**

The temperature controller is realized as a separate software thread inside the control software and can operate independently from the user interface if once started. It measures the actual temperature, calculates the actual temperature setpoint, using the above described model, and calculates the appropriate pulse width value for the switched heating/cooling source. The discrete PID controller equation is given by

$$U_k = U_{k-1} + (Q_0 * E_k + Q_1 * E_{k-1} + Q_2 * E_{k-2}) , \quad (5.40)$$

where  $U_k$  is the output value of the controller and  $U_{k-1}$  the last output

## 5.2 Frequency analysis of dynamic properties

value.  $E_k$  is the *error value* as given by

$$E_k = T_{Set} - T_{Meas} , \quad (5.41)$$

$E_{k-1}$  and  $E_{k-2}$  the former controller deviations.  $Q_0$ ,  $Q_1$  and  $Q_2$  are the controller parameters and defined as

$$Q_0 = P \cdot \left( 1.0 + \frac{T_d}{T_0} \right) \quad (5.42)$$

$$Q_1 = P \cdot \left( -1.0 + \frac{T_0}{T_i} - 2 \cdot \frac{T_d}{T_0} \right) \quad (5.43)$$

$$Q_2 = P \cdot \frac{T_d}{T_0} , \quad (5.44)$$

where  $P$  is proportional part,  $T_i$  the integration part,  $T_d$  the deviation part, and  $T_0$  the sample time of the controller.

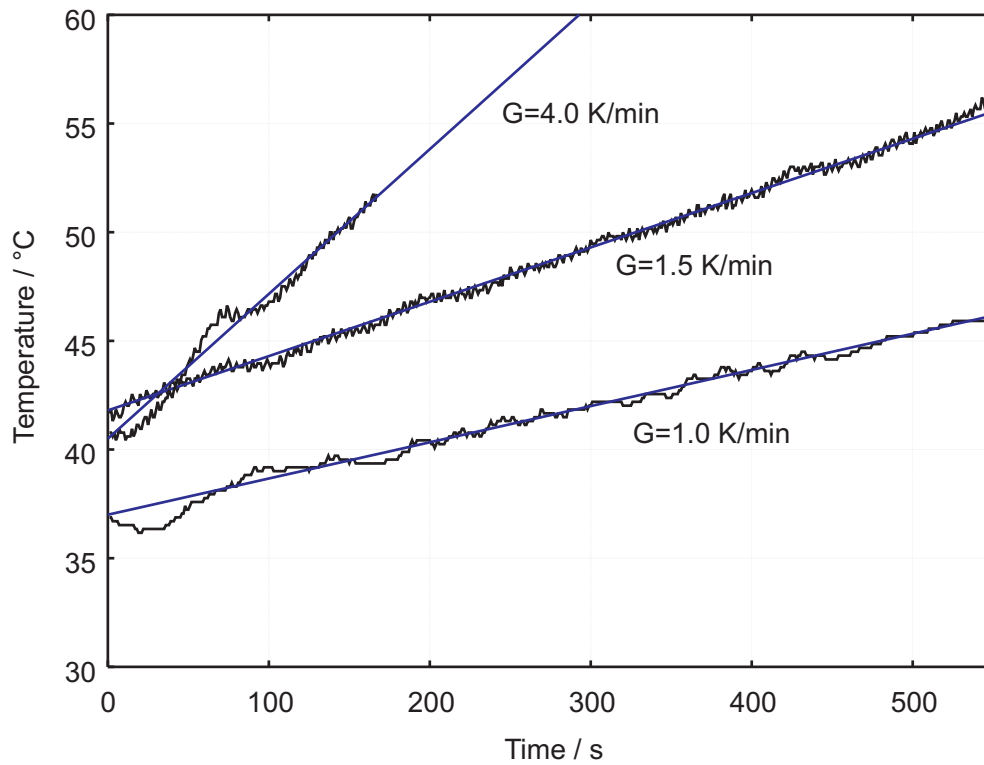


Figure 5.19: Temperature profiles

Fig. 5.19 shows temperature profiles with different temperature gradients. Especially for the big temperature gradient with  $G=4$  K/min, it is visible that, due to the heat capacity of the copper block, it takes some time at the beginning of the profile, until the actual temperature can follow the setpoint, but with the controller being in steady state the difference between the setpoint and the actual temperature is negligible.

### Instrument control and data interface

A customized field programming gate array (FPGA) is used in the realized instrument to control the different units of the instrument and establish a command and data exchange interface to the overall controlling PC.

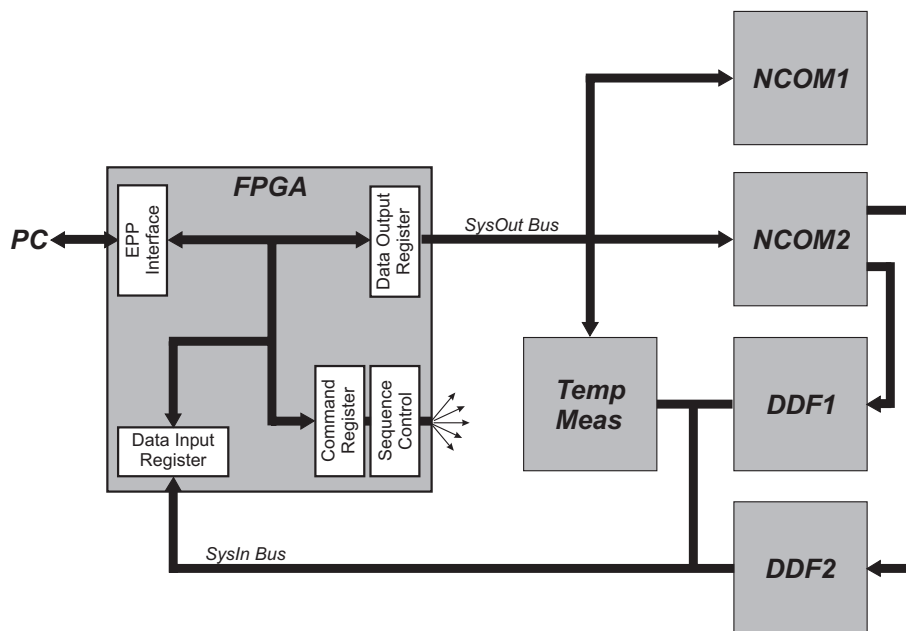


Figure 5.20: FPGA and system overview

A load&store architecture has been implemented within the FPGA to allow an easy but powerful control of the different devices integrated into the instrument. Fig. 5.20 shows a simplified overview of the realized FPGA structures and the bus connection to the main components.

The EPP interface implements the standard communications interface protocol for the parallel port of a PC, according to IEEE 1284. Data rates up to 1 MByte/s are obtainable using this protocol, which is sufficient for the present application. The 8 bit wide EPP-Bus is transformed to the 16 bit System Output Bus by two subsequent load operations of the *Data Output Register*. The *Command Register* is loaded for this purpose with the appropriate commands (*CMD\_LOAD\_LOW\_DATA\_REG*, *CMD\_LOAD\_HIGH\_DATA\_REG*). Further control of the instrument is simply done by copying the *Data Output Register* to one of the several target registers of the instrument. The complete configuration and operation feature set of the instrument is available by this scheme. Copying is initiated by loading the appropriate command into the *Command Register*. This triggers the *Sequence Control* for proper interfacing with the respective device. Reading of the data is performed by sampling the available data outputs of the instruments on command. The data are stored in registers inside the FPGA and can be transferred subsequently to the PC.

### 5.3 High resolution digital frequency analysis on polymers

Investigations on different polymers have been performed using the realized system. As an example, measurements on polymer blends, consisting of polystyrene, butyl acrylate and methacrylic acid, are presented in this section. Films with a thickness between  $50\mu\text{m}$  and  $100\mu\text{m}$  were prepared by spreading the polymer on a silicon surface. The films were vacuum dried and subsequently investigated with the SPM system. Temperature profiles with gradients between  $0.5\text{ K/min}$  and  $2\text{ K/min}$  were applied and the frequency response of the tip-polymer system were acquired every  $1\text{ K}$ .

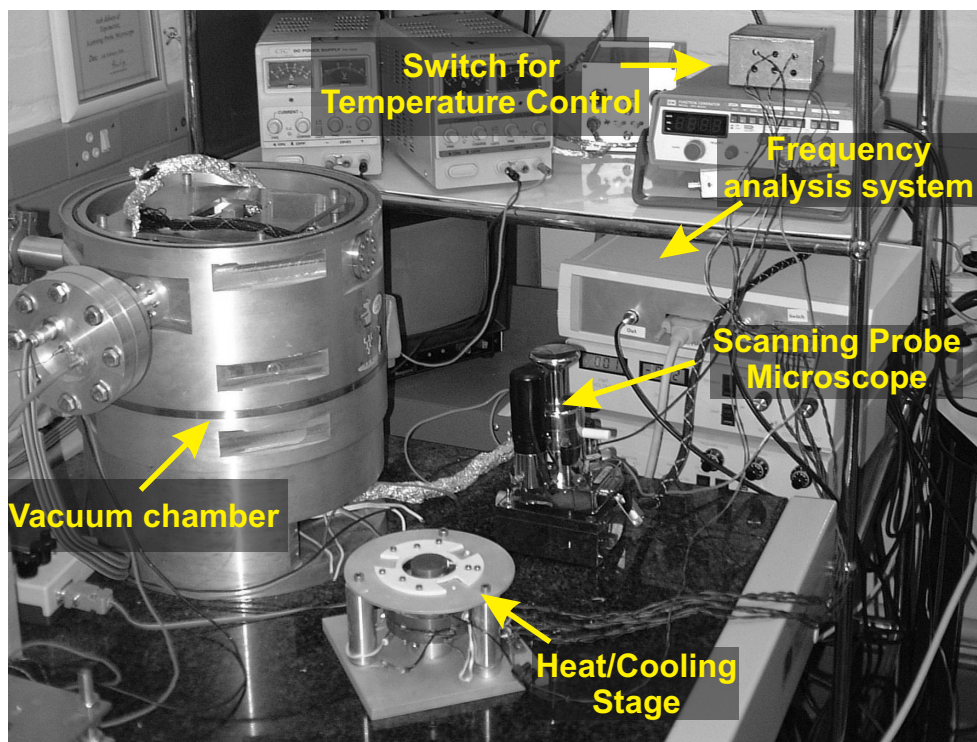


Figure 5.21: Setup for the investigation of polymers

### 5.3 High resolution digital frequency analysis on polymers

---

The setup of the digital analysis system for the investigation of polymers is shown in Fig. 5.21. A vacuum chamber is provided, which is used for the preparation of polymer films. The Scanning Probe Microscope and the heating/cooling stage can be built into the vacuum chamber, which allows the investigation at different ambient pressures. The measurements presented here were performed at normal pressure.

The magnitude response is shown for different temperatures in Fig. 5.22, while the phase response is presented in Fig. 5.23.

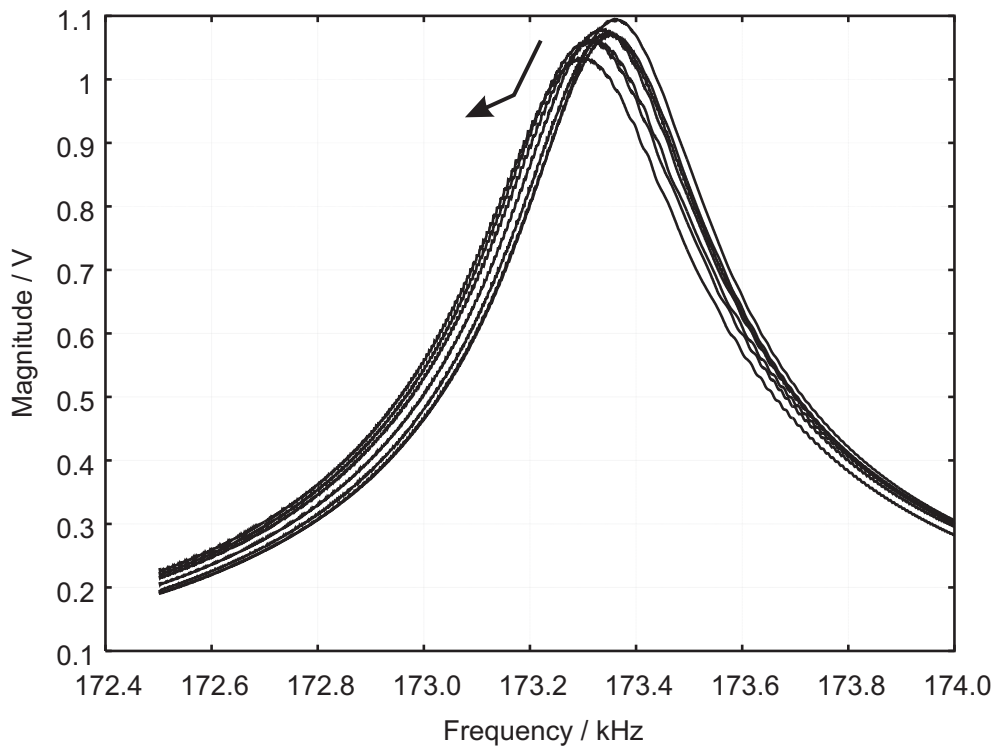


Figure 5.22: Magnitude response of the polymer film in dependency on temperature

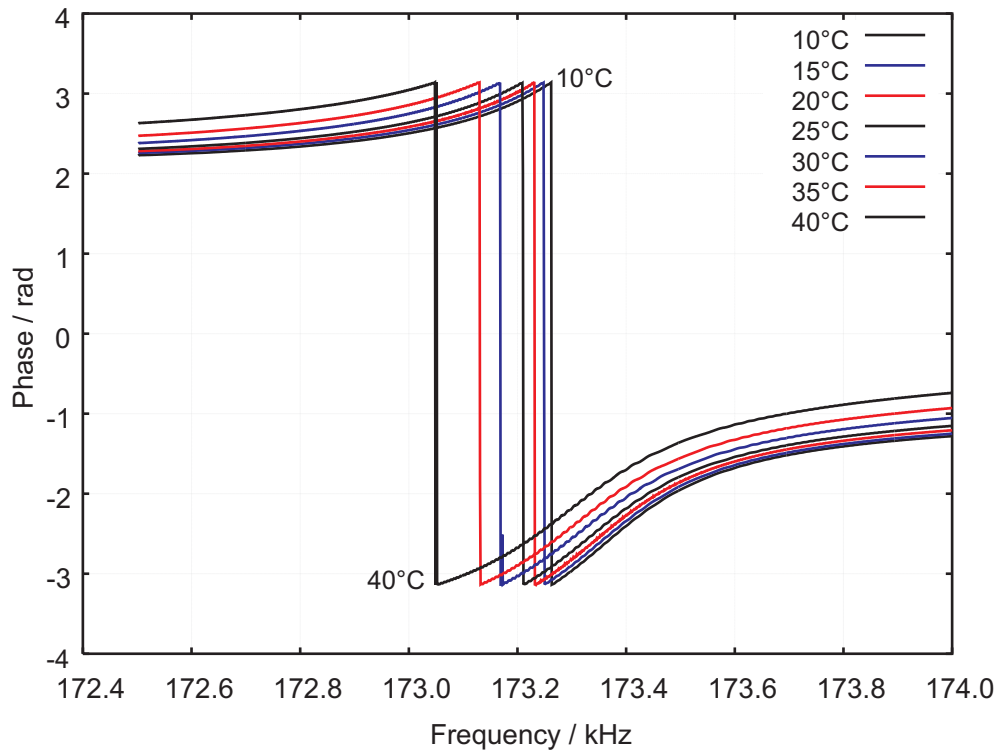


Figure 5.23: Phase response of the polymer film in dependency on temperature

These measurements show clearly, especially the phase image with the sharp transition from  $\pi$  to  $-\pi$ , that the resonance frequency of the cantilever is shifted to lower frequencies for increasing temperatures. According to chapter 2, this is caused by decreasing tip-polymer distance due to the volume expansion of the polymer. Additionally, in the temperature range associated with the glass transition of this polymer other influences are visible in the magnitude image. The here presented plots of the magnitude and phase response in dependency on temperature are originally converted to animation files, which allow the simultaneous investigation of different parameters like the

### 5.3 High resolution digital frequency analysis on polymers

---

magnitude of the resonance peak, the resonance frequency and the quality factor.

In these animations, increasing magnitude peaks around the glass transition regime are visible against the trend of the lowering amplitude vs distance. As it is not possible to show the animations adequately in printed form, different parameters have been extracted from the measured data and are plotted in the following figures.

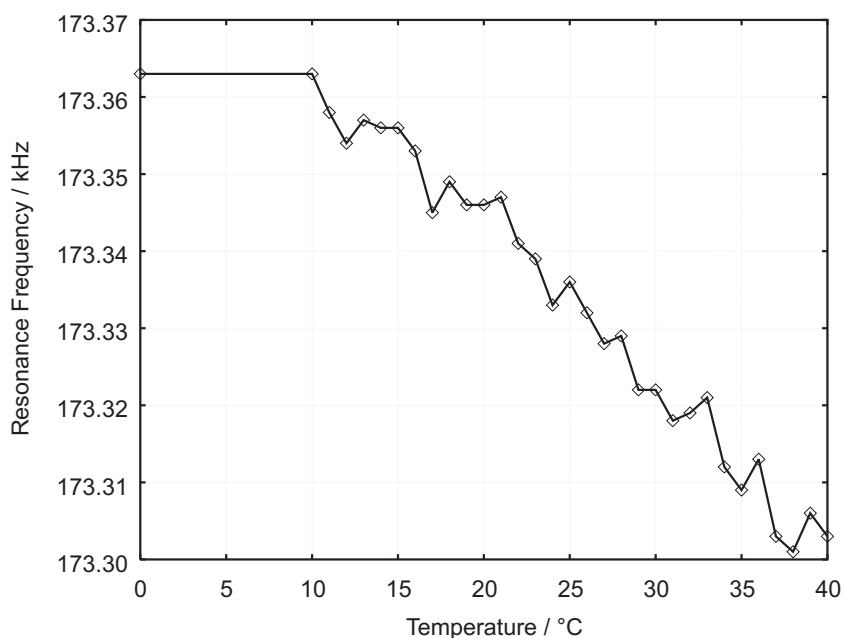


Figure 5.24: Resonance frequency dependency on temperature

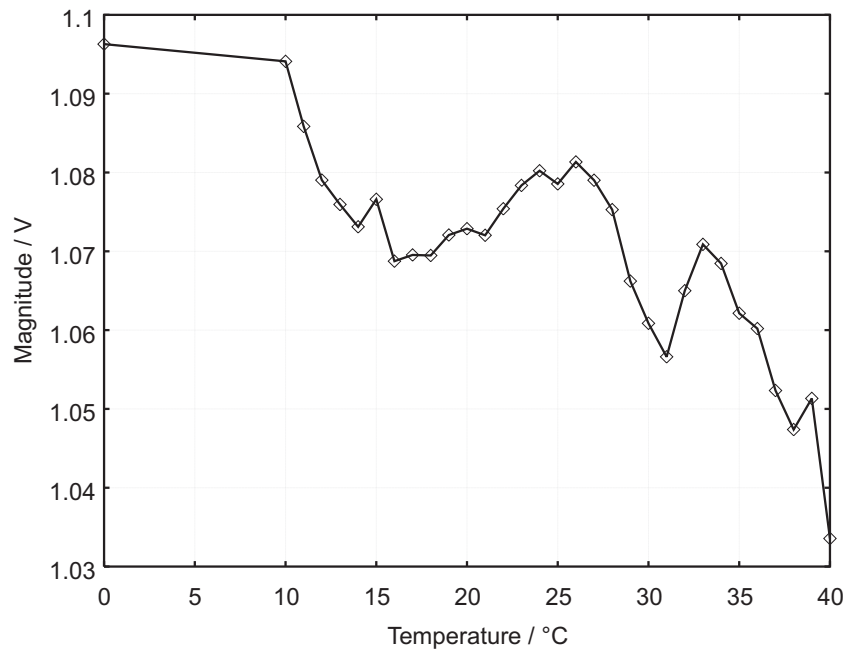


Figure 5.25: Magnitude dependency on temperature

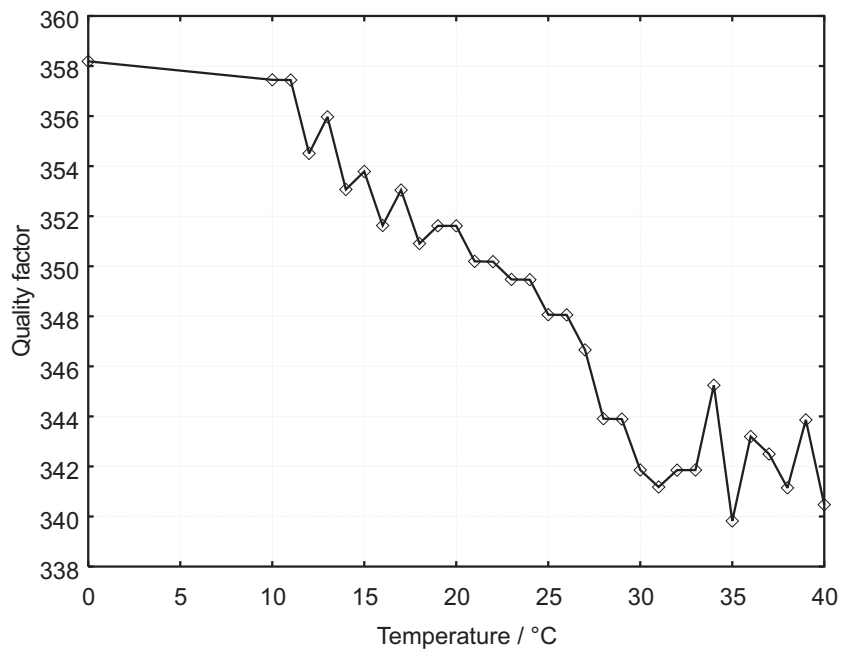


Figure 5.26: Quality factor dependency on temperature

Fig. 5.24 shows the resonance frequency as function of the temperature. It shows in this measurement a monotonic decrease, which can be described in good agreement to the intermolecular force theory by a decreasing tip-sample distance in the attractive force regime. Such a decreasing distance would also lead to a monotonic decrease of the vibration amplitude of the cantilever and also to a monotonic decrease of the quality factor. The plot of the resonance peak against the temperature, however, is not monotonic. At a temperature around 24°C, which is known from other measurements to be the glass transition temperature, the resonance peak has a local maximum. A second local maximum is observed at temperatures around 33°C. According to chapter 3, the chain mobility of polymers is increasing above the glass point. The different dipoles of the chain can arrange themselves in this range in different equal energetic configurations, varying thus the effective attractive force seen by the tip. This force fluctuation would affect the vibration behavior as seen in this measurement. Nevertheless the change of the vibration amplitude could be caused by other mechanisms, too. The main advantage of the here presented instrument is thus that it enables the systematic and reliable investigation of temperature dependent influences on the vibrating behavior of a cantilever in close proximity to a polymer film.



## 6 Conclusion

This work provides an extensive presentation of the realized high resolution digital frequency analysis system for the characterization of dynamic sample properties in Scanning Probe Microscopy. The realized system closes the gap between low-cost but simple frequency analysis solutions provided for SPM and the high-end but also high-price solutions, based on additional acquired network analysis hardware, often used in research laboratories for frequency analysis purposes.

The new system provides a frequency resolution of about 4 mHz with a signal-to-noise ratio of 135 dB, which allows the phase measurement with a resolution of  $(28 \cdot 10^{-6})^\circ$ . The system design is, based on theoretical and experimental investigation of the fundamental properties of commercial Scanning Probe Microscopes, optimized for the use in Scanning Probe Microscopy. Due to the flexible design, it is not limited to this purpose. The high frequency resolution was also used for the characterization of quartz tuning forks, which are becoming of increasing importance as high resolution force probes in Scanning Probe Microscopy.

The setup and handling of the instrument has been improved in comparison to other instruments, by an ease-of-use control software. A high level of automation in association with a rapid data acquisition allows a simple setup and transaction of various experiments. Especially the integrated control of arbitrary temperature profiles allows the automated investigation of dynamic samples properties in dependency of temperature, which opens up the field of characterization of thermomechanical properties in the micro/nanoscale. Exemplary measurements on polymers show that the investigation of characteristic parameters, like the glass transition temperature, is possible using this non-destructive method.

Beside the flexible system design the realized system cannot replace any existing frequency analysis system. Especially, no particular design precautions for the detection of weak signals, a domain of lock-in amplifiers, have been taken. The amplification of the analogue preamplifier is chosen to be around factor one, but as this preamplifier is realized on a separate add on board, a replacement of this preamp with a suitable one would enable the realized system also for signal recovery purposes. Furthermore the frequency range is limited due to design restriction. In the present system, the usable range is restricted by the software from 0 Hz to 1 MHz, which is more than sufficient for SPM applications. The overall achievable frequency range is determined by the system clock frequency and the desired clock to output frequency ratio. In the present realization the system clock frequency is chosen to be 20 MHz, which allows to cover a frequency range of up to 2 MHz, while maintaining a clock to output ratio of 10. As the relevant electronic devices are also available in 50 MHz versions, a

---

redesign of the board could extend the frequency range up to 5 MHz, assuming a minimum clock to output frequency ratio of 10.

## *6 Conclusion*

---

# Bibliography

- [1] Binnig, G. and Rohrer, H.: Scanning Tunneling Microscopy  
Helv. Phys. Acta **55** (1982), 726-735
  
- [2] The Royal Swedish Academy of Sciences: Official Press Release  
of the Nobel Foundation for the Nobel Prize in Physics 1986,  
<http://www.nobel.se/physics/laureates/1986/press.html>, 1986
  
- [3] Binnig, G.; Quate, C.F. and Gerber, Ch.: Atomic Force Microscope  
Phys. Rev. Letters **56** (1986), No. 9, 930-933
  
- [4] Gießibl, F.J.: Atomic Resolution of the Silicon (111)-(7x7) Surface  
by Atomic Force Microscopy  
Science **267** (1995), 68-71
  
- [5] Kitamura, S. and Masashi, I.: Observation of 7x7 Reconstructed  
Structure of the Silicon (111) Surface using Ultrahigh Vacuum  
Noncontact Atomic Force Microscopy  
Jpn. J. Appl. Phys. **34** (1995), Part 2, No. 1B, L145-L148
  
- [6] Martin, Y. and Williams, C.C.: Magnetic imaging by "force mi-

- croscopy" with 1000 Å resolution  
Appl. Phys. Lett. **50** (1987), No. 20, 1455-1457
- [7] Albrecht, T.R.; Grütter, P.; Horne, D. and Rugar, D.: Frequency modulation detection using high-Q cantilevers for enhanced force microscope sensitivity  
J. Appl. Phys. **69** (1991), No. 2, 668-673
- [8] Bonnel (Editor): Scanning Tunneling Microscopy and Spectroscopy: Theory, Techniques and Applications  
VCH Publishers, New York, 1993
- [9] Gotsmann, B.; Anczykowski, B.; Seidel, C. and Fuchs, H.: Determination of tip-sample interaction forces from measured dynamic force spectroscopy curves  
Appl. Surf. Science **140** (1999), 314-319
- [10] Oulevey, F.; Gremaud, G.; Sémoroz, A.; Kulik, A.J.; Burnham, N.A.; Dupas, E.; Gourdon, D.: Local Mechanical Spectroscopy with Nanometer Scale Lateral Resolution  
Rev. Sci. Instruments **69** (1998), 2085-2094
- [11] VanLandingham, M.R.; McKnight, S.H.; Palmese, G.R., Huang, X.; Bogetti, T.A., Eduljee, R.F. and Gillespie: Nanoscale Indentation of Polymer Systems Using the Atomic Force Microscope  
Journal of Adhesion **64** (1997), 31-59
- [12] Krottil, H.U.; Stifter, T.; Waschipky, H.; Weishaupt, K.; Hild, S. and Marti, O.: Pulsed Force Mode: A New Method for the Investigation of Surface Properties  
Surface and Interface Analysis **27** (1999), 336-340

- [13] Marti, O; Stifter, T.; Waschipky, H.; Quintus, M. and Hild, S.:  
Scanning Probe Microscopy of heterogeneous polymers  
*Colloids & Surfaces A* **154** (1999), 65-73
- [14] Fischer, T.E.; Marszalek, P.E.; Oberhauser, A.F.; Carrion-  
Vazquez, M. and Fernandez,J.M.: The micro-mechanics of single  
molecules studied with atomic force microscopy  
*Journal of Physiology* **520** (1999), No. 1, 5-14
- [15] Carrion-Vazquez, M.; Oberhauser, A.F.; Fowler, S.B.; Marszalek,  
P.E.; Broedel, S.E.; Clarke, J. and Fernandez,J.M.: Mechanical  
and chemical unfolding of a single protein: A comparison  
*Biophysics* **96** (1999), 3694-3699
- [16] Cuberes, T.; Assender, H.E.; Briggs, G.A.D.; and Kolosov, O.V.:  
Heterodyne force microscopy of PMMA/rubber nanocomposites:  
nanomapping of viscoelastic response at ultrasonic frequencies  
*J. Appl. Phys.* **33** (1999), 2347-2355
- [17] Fiege, G.B.M: Quantitative Erfassung von thermischen Eigen-  
schaften mit Hilfe der Rastersondenmikroskopie  
PhD Thesis, University of Wuppertal, Germany, 2001
- [18] Kajiyama, T.; Tanaka, K. and Takahara, A.: Study of the sur-  
face glass transition behaviour of amorphous polymer film by  
scanning-force microscopy and surface spectroscopy  
*Polymer* **39** (1997), No. 19, 4665-4673
- [19] Overney, R.M.; Buenviaje, C.; Luginbühl, R. and Dinelli, F.:  
Glass and Structural Transitions measured at polymer surfaces  
on the nanoscale  
*Journal of Thermal Analysis and Calorimetry* **59** (2000), 205-225

## *Bibliography*

---

- [20] Oulevey, F.; Burnham, N.A.; Gremaud, G.; Kulik, A.J.; Pollock, H.M.; Hammiche, A.; Reading, M.; Song, M. and Hourston, D.J.:  
Dynamic mechanical analysis at the submicron scale  
*Polymer* **41** (2000), 3087-3092
- [21] Meincken, M.; Balk, L.J. and Sanderson, R.D.: Improved Sensitivity in the Thermal Investigation of Polymeric Nanophases by Measuring the Resonance Frequency Shift using an Atomic Force Microscope  
*Macromol. Mater. Eng.* **286** (2001), No. 7, 412-420
- [22] Petersen, C.; Heldmann, C. and Johannsmann, D.: Internal Stresses during Film Formation of Polymer Lattices  
*Langmuir* **15** (1999), 7745-7751
- [23] Sarid, D.: *Scanning Force Microscopy*  
Oxford University Press, 1991
- [24] Colton, R.J.; Engel, A.; Frommer, J.; Gaub, H.E.; Gewirth, A.A.; Guckenberger, R.; Heckl, W.; Parkinson, B. and Rabe, J. (Editors): *Procedures in Scanning Probe Microscopy*  
John Wiley & Sons, 1998
- [25] *Nanosensors Product Guide 05/99*  
Nanosensors Dr. Olaf Wolter GmbH, Wetzlar, 1999
- [26] *Nanosensors Online Catalogue*  
<http://www.nanosensors.com>, 2002
- [27] Thie, M. and Denker, H.W.: Examining the molecular interaction between two cells: adhesion forces between the free surface of uterine epithelium and trophoblast

Presented at the 31. Kolloquium des Arbeitskreises für Elektronenmikroskopische Direktabbildung und Analyse von Oberflächen, Saarbrücken, 1998

- [28] Kuchling, H: Taschenbuch der Physik  
Verlag Harri Deutsch, 1989
- [29] WebElements - The Periodic Table on the WWW  
<http://www.webelements.com>, 2002
- [30] Hutter, J.L. and Bechhoefer, J.: Calibration of atomic-force microscope tips  
Rev. Sci. Instrum. **64** (1993), No. 7, 1868-1873
- [31] Sader, J.E.; Larson, I.; Mulvaney, P. and White, L.R.: Method for the calibration of atomic force microscope cantilevers  
Rev. Sci. Instrum. **66** (1995), No. 7, 3789-3798
- [32] Walters, D.A; Cleveland, J.P.; Thomson, N.H.; Hansma, P.K.; Wendman, M.A., Gurley, G. and Elings, V.: Short cantilevers for atomic force microscopy  
Rev. Sci. Instrum. **67** (1996), No. 10, 3583-3590
- [33] Proksch, R. and Cleveland, J.: Quantifying Molecular Forces: Sensitivities and Spring Constants without Touching a Surface  
Presented at STM 2001
- [34] Hamamatsu: Two-dimensional PSD Datasheet, S1200 et al.  
Online Datasheet at <http://www.hamatsu.de>  
Hamamatsu Photonics Deutschland GmbH, Herrsching, Germany, 2002

## *Bibliography*

---

- [35] Hamamatsu: Photodiodes Catalogue  
Hamamatsu Photonics Deutschland GmbH, Herrsching, Germany, 2000
- [36] Centrovision: Electrical/Optical Specification of Series 29 Specialty Photodiodes, CD-33H-2D  
Online Specifications at <http://www.centrovision.com>  
Thermo Centro Vision Inc., Newbury Park, USA, 2002
- [37] Centrovision Online Publication: A Primer on Photodiode Technology  
<http://www.centrovision.com>  
Thermo Centro Vision Inc., Newbury Park, USA, 2002
- [38] Siemens: Halbleiter - Technische Erläuterungen und Kenndaten für Studierende  
Siemens Aktiengesellschaft, Berlin und München, Germany, 1990
- [39] Hering, E; Martin, R.; Stohrer, M.: Physik für Ingenieure  
VDI-Verlag, Düsseldorf, Germany, 1989
- [40] Klein, J.W.; Dullenkopf, P.; Glasmachers, A.: Elektronische Meßtechnik - Meßsysteme und Schaltungen  
B.G. Teubner, Stuttgart, 1992
- [41] Texas Instruments: Datasheet of the TL054 Operation Amplifier  
Texas Instruments, 2002
- [42] Hicks, T.R.; Atherton, P.D.: The NanoPositioning Book - Moving and Measuring better than a Nanometre  
Queensgate Instruments, Berkshire, UK, 1997

- [43] Physik Instrumente GmbH: MicroPositioning, NanoPositioning, NanoAutomation - Solutions for Cutting-Edge Technologies  
Physik Instrumente, Karlsruhe, Germany, 2001
- [44] Jendritza, D.J. et al.: Technischer Einsatz Neuer Aktoren - Grundlagen, Werkstoffe, Designregeln und Anwendungsbeispiele  
Expert Verlag, Renningen-Malmsheim, Germany, 1995
- [45] Liu, X.X.: Microanalyses of Ferroelectric Properties of BaTiO<sub>3</sub>  
PhD Thesis, University of Wuppertal, Germany, 2001
- [46] Israelachvili, J.N.: Intermolecular and Surface Forces  
Academic Press, San Diego, USA, 1989
- [47] Burnham, N.A. and Kulik A.J., Handbook of Micro/Nanotribology (Editor: Bhushan, B.)  
Chapter 5: Surface Forces and Adhesion  
CRC Press, Boca Raton, USA, 1997
- [48] Sokolov, I.Y, Henderson, G.S. and Wicks, F.J.: Theoretical and experimental evidence for "true" atomic resolution under non-vacuum considerations  
Journal of Applied Physics **86** (1999), No. 10, 5537-5540
- [49] Burnham, N.A.; Behrend, O.P.; Oulevey, F.; Gremaud, G.; Gallo, P.J.; Gourdon, D.; Dupas, E.; Kulik, A.J.; Pollock, H.M. and Briggs, G.A.D.: How does a tip tap?  
Nanotechnology **8** (1996), 67-75
- [50] Gießibl, F.J.: Forces and frequency shifts in atomic-resolution

- dynamic-force microscopy  
Physical Review B **56** (1997), No. 24, 16010-16015
- [51] Livshits, A.I.; Shluger, A.L. and Rohl, A.L.: Contrast mechanism in non-contact SFM imaging of ionic surfaces  
Applied Surface Science **140** (1998), 327-332
- [52] Gießibl, F.J.; Bielefeldt, H.; Hembacher, S. and Mannhart, J.: Calculation of the optimal imaging parameters for frequency modulation atomic force microscopy  
Applied Surface Science **140** (1998), 352-357
- [53] Morita, S. and Sugawara, Y.: Guidelines for the achievement of true atomic resolution with noncontact atomic force microscopy  
Applied Surface Science **140** (1998), 406-410
- [54] Livshits, A.I. and Shluger, A.L.: Atomic and chemical resolution in scanning force microscopy on ionic surfaces  
Applied Surface Science **141** (1998), 274-286
- [55] Fontaine, P.; Guenoun, P. and Daillant, J.: A critical look at surface force measurement using a commercial atomic force microscope in the noncontact mode  
Rev.Sci.Instrum. **68** (1997), No. 11, 4145-4151
- [56] Lévêque, G.; Girard, P.; Belaidi, S. and Cohen Solal, G.: Effects of air damping in noncontact resonant force microscopy  
Rev.Sci.Instrum. **68** (1997), No. 11, 4137-4144
- [57] Hirserkorn, S.; Rabe, U. and Arnold, W.: Theoretical description of the transfer of vibration from a sample to the cantilever of an

- atomic force microscope  
Nanotechnology **8**, 1997, 57-66
- [58] Cleveland, J.P.; Anczykowski, B.; Schmid, A.E. and Elings, V.B.:  
Energy dissipation in tapping-mode atomic force microscopy  
Applied Physics Letters **72**, No 20, 1998, 2613-2615
- [59] Anczykowski, B.; Gotsmann, B; Fuchs, H.; Cleveland, J.P. and Elings, V.B.: How to measure energy dissipation in dynamic mode atomic force microscopy  
Applied Surface Science **140**, 1999, 376-382
- [60] Gießibl, F.J.: Rasterkraftmikroskop sieht erstmals ins Innere des Atoms  
Spektrum der Wissenschaft **04**, 2001, 12-14
- [61] Brigham, E.O.: FFT : Schnelle Fourier-Transformation  
Oldenburg, München, Germany, 1995
- [62] Gerdson, P. and Kröger, P.: Digitale Signalverarbeitung in der Nachrichtenübertragung  
Springer-Verlag, Berlin – Heidelberg – New York, Germany, 1997
- [63] Tektronix Online Application Note: Spektralanalyse: Analyse eines Signalspektrums  
<http://www.tektronix.com>
- [64] LeCroy: Waverunner Operator's Manual  
LeCroy Corporation, Chestnut Ridge, USA, 2000
- [65] Stanford Research Systems Application Note: About FFT Spectrum Analyzers

## *Bibliography*

---

- Scientific and Engineering Instruments, Stanford Research Systems, Sunnyvale, USA, 1996
- [66] Stanford Research Systems Application Note: About Lock-In Amplifiers  
Scientific and Engineering Instruments, Stanford Research Systems, Sunnyvale, USA, 1996
- [67] Bronstein, I.N. and Semendjajew, K.A.: Taschenbuch der Mathematik  
B.G. Teubner Verlag, Leipzig – Stuttgart, Germany, 1991
- [68] Agilent: Agilent 4396B 1.8 GHz Network/Spectrum Analyzer – Data Sheet Agilent Technologies, 2002
- [69] Agilent: Introducing the Agilent 4395B Agilent Technologies, 2002
- [70] Cowie, J.M.G.: Chemie und Physik der synthetischen Polymeren – Ein Lehrbuch  
Vieweg Verlag, Braunschweig, Wiesbaden, 1997
- [71] TA Instruments Product Information: DSC 2920 – Differential Scanning Calorimeter  
TA Instruments Inc., New Castle, DE, 2001
- [72] TA Instruments Product Information: DMA 2980 – Dynamic Mechanical Analyzer  
TA Instruments Inc., New Castle, DE, 2001
- [73] TA Instruments Product Information: DEA 2970 – Dielectric Analyzer  
TA Instruments Inc., New Castle, DE, 2001

- [74] Häßler, R.: Modulierte Dynamische Differenzkalorimetrie – Neue Anwendungsmöglichkeiten auf dem Gebiet der Epoxidharze  
Farbe & Lack **104** (1998), No. 10 , 93-98
- [75] Krottil, H.U.; Weilandt, E.; Stifter, Th.; Marti, O. and Hild, S.: Dynamic Friction Force Measurement with the Scanning Force Microscope  
Surface and Interface Analysis **27** (1999), 341-347
- [76] Intersil Datasheet: HSP 45116 – Numeric Controlled Oscillator/Modulator  
Intersil Corporation (1999), <http://www.intersil.com>
- [77] Karrai, K. and Grober, R.D.: Piezoelectric tip-sample distance control for near field optical microscopes  
Appl. Phys. Lett. **66** (14), 1995
- [78] Cramer, R.M: Dedicated Near-Field Optical Microscopies for Semiconductor Materials and Devices  
PhD Thesis, University of Wuppertal, Germany, 1999
- [79] Gießibl, F.J.: High-speed force sensor for force microscopy and profilometry utilizing a quartz tuning fork  
Appl. Phys. Lett. **73** (26), 1998

## Acknowledgments

I would like to thank Prof. Dr. Ludwig Josef Balk for the opportunity to carry out this work at his Department of Electronics at the University of Wuppertal and for attendance and encouragement I've gotten in this time.

Thank you very much to Prof. Dr. Albrecht Glasmachers for taking over the second expertise, for his interest and support of the work. His friendly and helpful nature will stay very pleasant in my mind.

I would like to thank Prof. Dr. Ronald D. Sanderson for the opportunity to carry out a part of my work at his Institute for Polymer Science at the University of Stellenbosch.

Thank you very much also to my colleagues at the department, Andreas Altes, Ronald Cramer, Volker Feige, Ingo Joachimsthaler, Ansgar Körbes, Xiao Xia Liu and especially Gero Fiege and Ralf Heiderhoff for the time we spent together, helpful discussions and support I've gotten in this time.

A special thank you to the present and future doctors Sevki Gencol, Peter Muß, Darko Rozic and Michael Schugt for valuable discussions and friendly support and encouragement.

Thank you very much also to the secretaries, and here I wish to say thank you to Mrs. Mechthild Knippschild and Mrs. Jutta Winter for settling a lot of "routine" work, making workaday routine evidently more pleasant.

Beside the above mentioned people, there are a lot more people I have

to say thank you to, but I would always run in danger to forget some of them trying to enumerate them here personally. Nevertheless thank you very much, I think you know who you are.